

7 Beam Delivery System

7.1 Introduction

The Beam Delivery System (BDS) transports the beams from the exit of the linacs to the interaction point (IP), where they are brought into collision, and then safely extracted and dumped in high-power beam dumps. The BDS serves several important functions. It must:

- produce the necessary strong demagnification of the beams, resulting in the $550\text{ nm}\times 5\text{ nm}$ beam spots at the IP;
- maintain the beams in collision using active stabilisation (feedback);
- cleanly extract the strongly disrupted beams after the IP, and transport them to high-power dumps;
- provide a high level of machine (and detector) protection, in the event of a linac fault resulting in a beam with either a large energy error or a large orbit deviation or both;
- provide collimation of large amplitude particles (the so-called beam halo) coming out of the linac, which would cause significant background in the physics detector;
- provide diagnostics (emittance measurement) for the linac;
- include a switch-yard to separate the beamline serving the (optional) second interaction region (IR).

In addition to the above, the *electron* BDS must also accommodate the undulator-based positron source (section 4.3), which is located at the exit of the electron linac.

In this chapter, an overview of the TESLA BDS sub-systems is given. Many of the basic concepts and design constraints have been covered in the original Conceptual Design Report (CDR)[83]: since then, however, new concepts and philosophies have been adopted, and the system described here is significantly different from the one described in the CDR. The chapter is divided into seven sections which reflect the primary functions of the BDS:

- Section 7.2 acts as an introduction to the entire system, covering the lattice, optics, magnets and vacuum systems.

- Section 7.3 covers the luminosity stability issues, with emphasis on the various feedback systems that need to be implemented in order to achieve the required high luminosity. Effects of vibration and ground motion are also discussed.
- Section 7.4 deals with the important considerations related to the IR (machine-detector interface), and particular beam-beam effects.
- Section 7.5 gives an overview of the beam halo collimation system, which uses mechanical spoilers to physically ‘scrape’ the halo particles off the beam. Machine protection issues are also covered in this section.
- Section 7.6 discusses both the charged-particle spent-beam extraction system and the beamstrahlung extraction system.
- Finally, section 7.7 covers the concept and design of the high-power main beam dump.

The chapter is intended to be a comprehensive overview of the current design and philosophy of the TESLA BDS: more detailed information on particular sub-systems or components can be found in the supplied references.

7.2 Magnet Lattice and Optics

The following sections provide an overview of the main features of the primary e^+e^- BDS up to the IP. The main extraction line system will be dealt with separately in section 7.7.

7.2.1 Basic layout and geometry

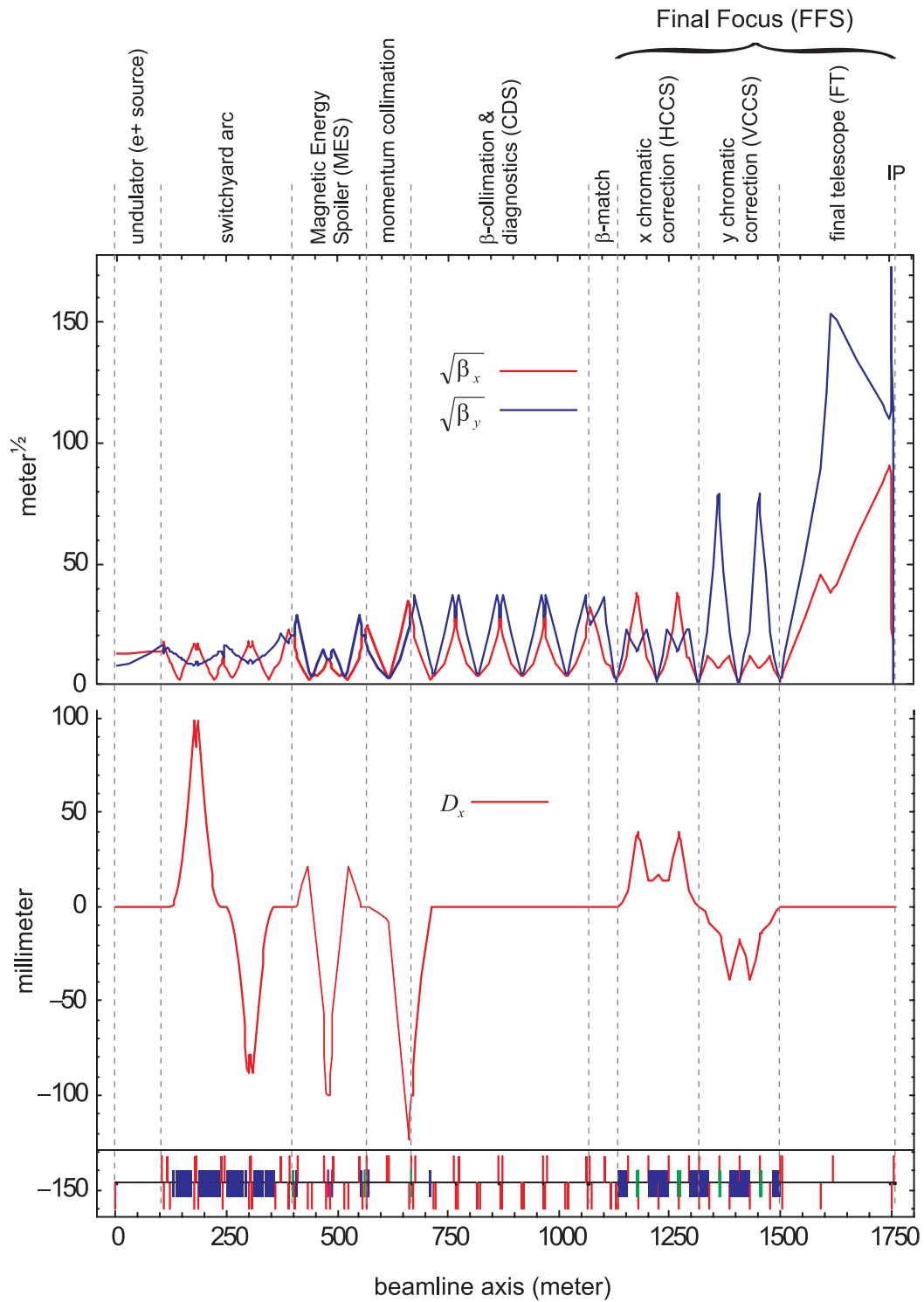
The TESLA BDS for the primary e^+e^- IR is 3436 m in length (linac to linac). The IR itself sits slightly off-centre, with the e^- and e^+ delivery systems being 1759 m and 1677 m in length respectively. The slight asymmetry is due to the undulator-based e^+ source at the exit of the e^- linac (section 4.3). From the first bend magnet in the switch-yard (section 7.2.2) both lattices are identical.

Figure 7.2.1 plots $\sqrt{\beta_{x,y}}$ and the dispersion function (D_x) for the BDS (e^-). The various modules which separate out the functionality of the BDS are clearly marked:

e^+ source undulator Contains space for the e^+ source undulator (section 7.2.2).

Switch-yard Arc A double bend achromat arc which acts as a switch to a second IR and allows enough clearance for the e^+ source photon target (section 7.2.2).

Magnetic Energy Spoiler (MES) A dispersive section containing non-linear elements which ‘blow up’ the beam at the downstream energy collimator in the event of a large energy error (section 7.2.3).

Figure 7.2.1: Optics functions for the TESLA BDS (e^-).

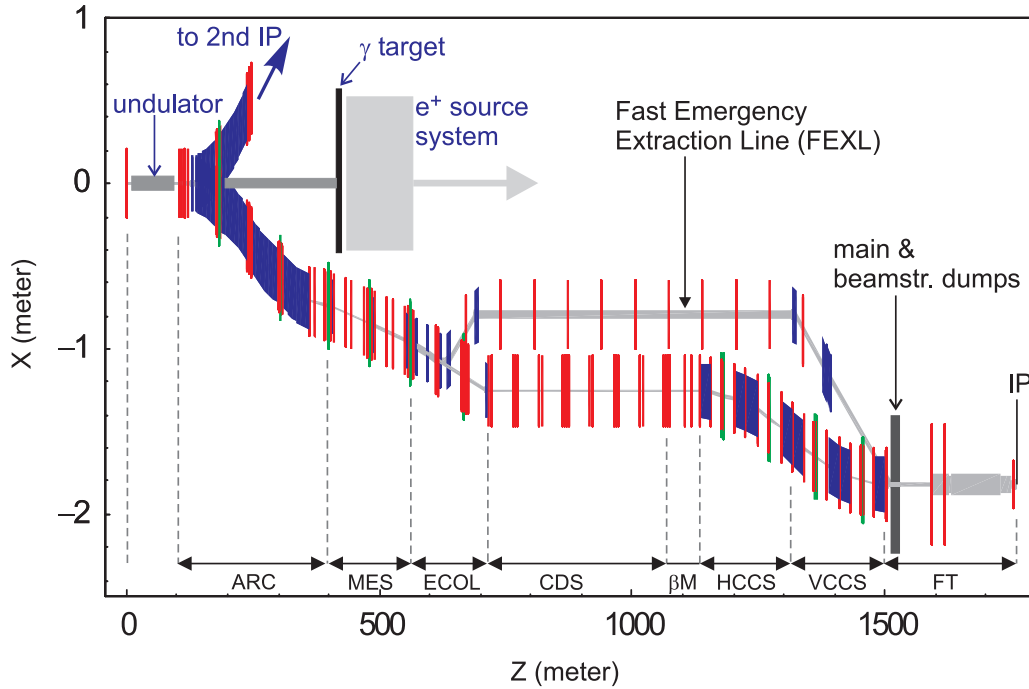


Figure 7.2.2: Geometry of the primary e^- BDS from linac to IP.

Momentum Collimation A point of high dispersion where the primary energy collimator will be placed (section 7.2.3).

Collimation and Diagnostics Section (CDS) A repetitive lattice where a series of spoilers and absorbers are used to collimate the beam halo. This section will also support the primary emittance measurement station (section 7.2.4).

β -Match Matching from the CDS to the entrance (image point) of the Final Focus System.

Final Focus System (FFS) A second-order achromatic telescope system which focuses the beam at the IP (section 7.2.5).

Figure 7.2.2 shows the geometry of the electron BDS, including the Fast Emergency Extraction Line (FEXL, section 7.2.6), and an indication of the location of the positron source system (section 4.3). The IP has a transverse offset with respect to the linac of 1.82 m, and the net bending angle is zero. Figure 7.2.3 shows the complete BDS layout (linac to linac), including the optional second IR.

7.2.2 Positron source undulator and beam switch-yard

In the case of the e^- BDS, the undulator for the e^+ source is installed directly after the linac. The matching from linac to undulator is designed to reduce the e^- phase space contribution to the total photon spot size at the target to less than one-fifth (a

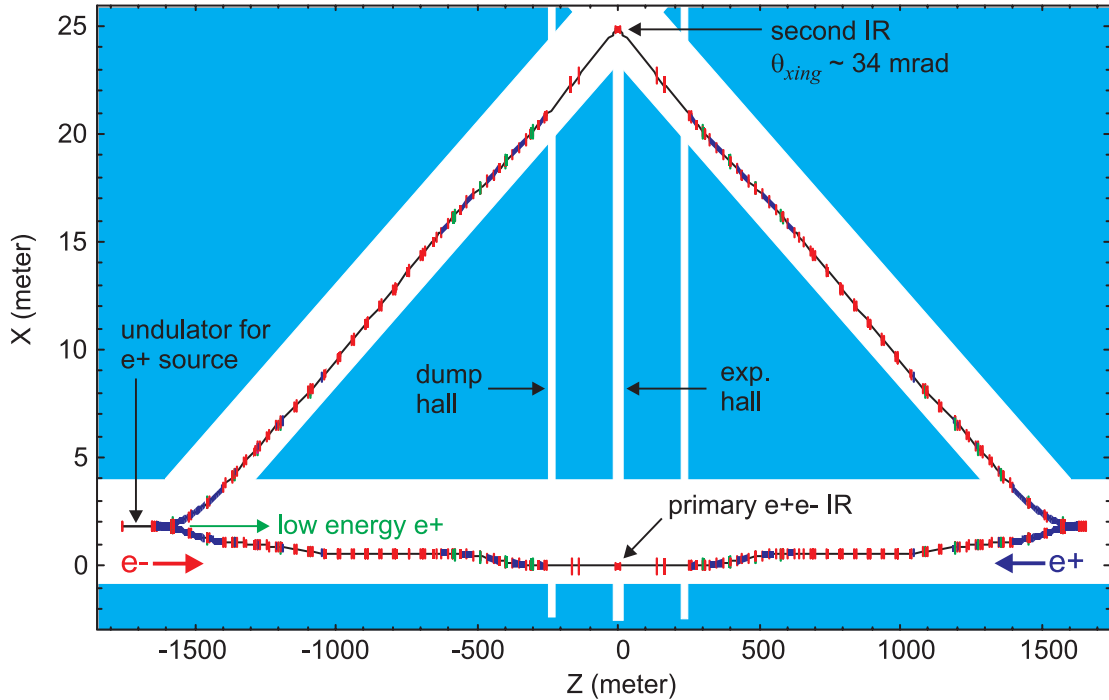


Figure 7.2.3: *Geometry of the TESLA BDS, including the second IR.*

necessary constraint for polarised e^+ production). Details of the e^+ source are covered in section section 4.3. The undulator increases the relative energy spread in the beam to about 0.15%, as compared to $< 0.05\%$ coming out of the linac; this increase has consequences for the magnet stability tolerances and luminosity stabilisation (section 7.3).

Immediately after the undulator, the beam switch-yard steers the e^- beam to either of the two foreseen interaction regions (figure 7.2.4). The switch-yard is placed after the undulator so as not to exclude the possibility of e^+e^- collisions at the second IR. The two primary constraints for the design of the switch-yard arcs are:

- the emittance growth due to synchrotron radiation should be kept to an acceptable minimum; and
- the arc geometry should allow enough clearance for the photon target and the associated e^+ capture system (section 4.3).

The first 24 dipole magnets are common to both beamlines, after which the transverse clearance is enough to separate the two (see 7.2.7 for magnet details). The use of iron-core electromagnets precludes fast intra-bunch switching between the two IRs, but could in principle allow switching at 5 Hz.

The lattice is based on a double-bend achromat system used in modern light sources to significantly reduce the horizontal emittance growth from synchrotron radiation effects. Figure 7.2.5 shows the emittance growth along the entire BDS beamline: the

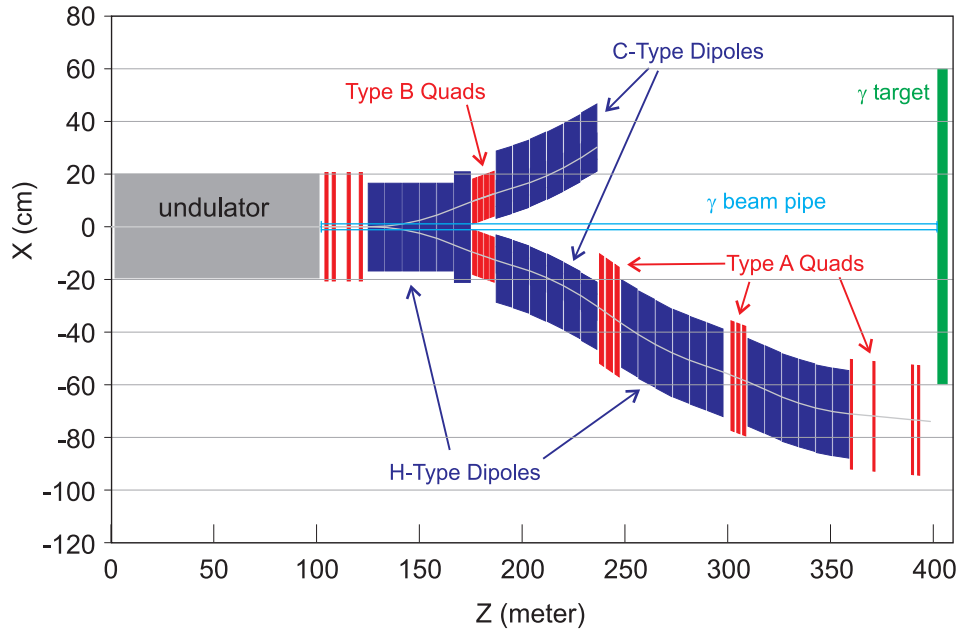


Figure 7.2.4: The BDS switch-yard, showing the location of the photon beamline and target.

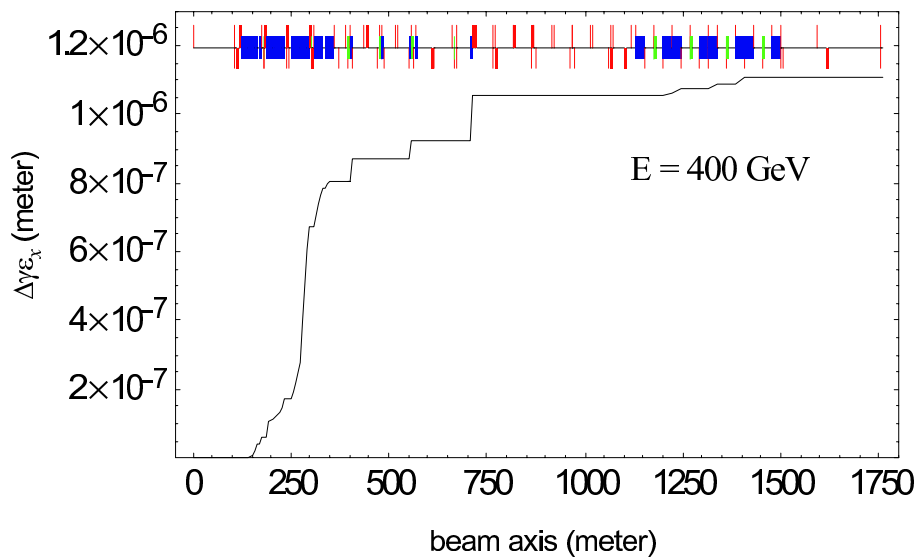


Figure 7.2.5: Horizontal emittance growth for the entire BDS, and a beam energy of 400 GeV (design emittance $\gamma\epsilon_x = 8 \times 10^{-6}$ m).

largest contribution comes from the arcs, but the total effect is still less than 14% at 400 GeV which is considered acceptable.

A complete and detailed description of the BDS switch-yard system can be found in [2].

7.2.3 Energy collimation and magnetic energy spoiler (MES)

The system is characterised by the double peaked dispersion function (after the switchyard arc, see figure 7.2.1). The first peak is the so-called magnetic energy spoiler (MES), which forms part of the machine protection (MP) system. It is primarily intended to protect the downstream (mechanical) energy spoiler from being damaged by a direct hit from an off-energy beam. In the event of a beam energy error ($>2\%$), The MES serves two related MP functions:

- a BPM placed at the high dispersion peak is used to send a signal to the downstream fast kicker system of the Fast Emergency Extraction Line (FEXL, section 7.2.6), causing the remainder of the bunch train to be safely extracted to the main dump;
- the non-linear magnets in the system significantly increase the vertical beam size on the face of the downstream energy spoiler, allowing the spoiler to survive a few bunches from the train.

Section 7.5 covers the collimation system in more detail, while the FEXL is covered in section 7.2.6.

7.2.4 Collimation and diagnostics section (CDS)

In the CDR [83] version of the BDS, the collimation system and diagnostic sections were separated. In the current system, the betatron collimation system and the main emittance measurement station have been combined into a single beamline. Betatron collimation is now performed at intervals of 45° phase advance, at locations of relatively large beam size ($\sigma_{x,y} = 127,7 \mu\text{m}$ at 250 GeV). Such a lattice also provides for an efficient emittance measurement station as described in [4], using profile monitors close to each spoiler location. For the monitors themselves, both flying carbon-wire monitors [5] and laser-wires [6] are envisaged, the latter being used during nominal luminosity (high current) operation. A more detailed description of the lattice can be found in section 7.5.

7.2.5 Final focus system (FFS)

The FFS focuses the beams down to the required $\sigma_x = 550 \text{ nm}$ and $\sigma_y = 5 \text{ nm}$ at the IP (250 GeV). The optics is based on that used for the SLC final focus system [7] and the final focus test beam (FFTB) [8]. The demagnification is performed by a point-to-point telescope system (Final Telescope, FT). Upstream of the FT are two dispersive sections referred to as the horizontal (HCCS) and vertical (VCCS) chromatic correction sections, where pairs of strong sextupoles separated by a $-I$ transformation are used to correct (to second-order) the strong chromaticity of the final doublet. Figure 7.2.6 shows the momentum bandwidth for the BDS; the bandwidth due only to the FFS is also shown for comparison.

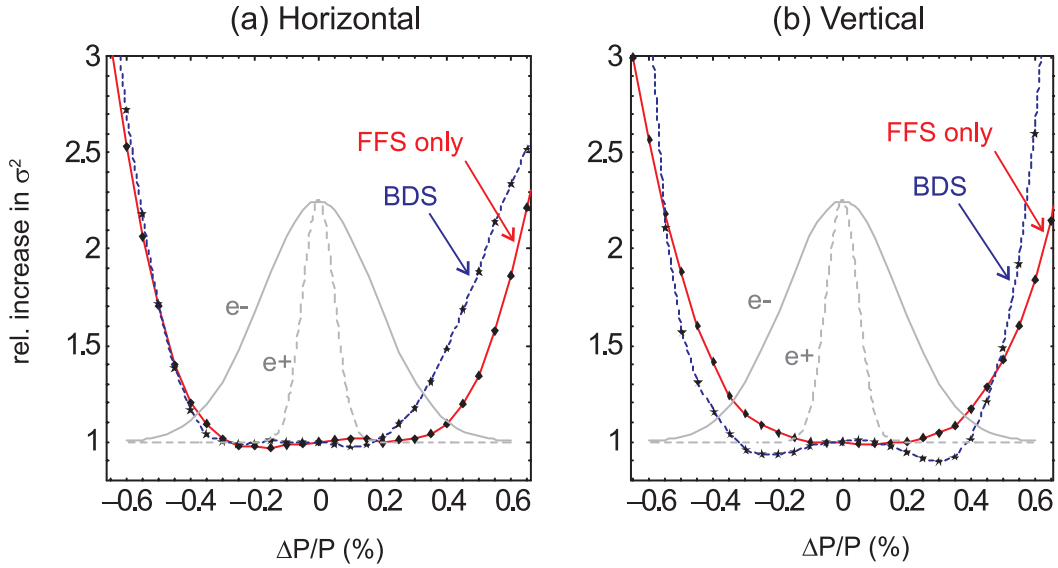


Figure 7.2.6: Energy bandwidth for the (a) horizontal and (b) vertical plane. The bandwidth for the entire BDS and only the FFS are indicated. The energy profile of both e^- and e^+ are also shown for comparison.

To allow a clear extraction path for the beamstrahlung to the main dump hall (~ 250 m from the IP), the length of the FT has been significantly increased beyond that which would naturally be required (see section 7.7). In order to re-establish the correct optics and required bandwidth, an additional weak doublet is now required approximately 130 m upstream of the final doublet. The length of the FFS system is now approximately 700 m long, compared to ~ 500 m for the system described in the CDR [83].

7.2.6 Fast emergency extraction line (FEXL)

The fast emergency extraction line is primarily intended to extract the remainder of the bunch train safely to the main dump (section 7.7) in the event of a machine protection trip. In addition, it will serve as a by-pass system during commissioning. Figure 7.2.7 shows the overall concept of the FEXL, while the exact geometry can be seen in figure 7.2.2.

The extraction point for the FEXL is placed just downstream of the MES (section 7.5.3). Should an off-energy bunch train exit the linac ($|\Delta E/E| > 2\%$), the BPM at the non-zero dispersive point in the MES can send a signal to the fast kicker system, approximately 80 m downstream¹. Since the signal and beam travel in the same direction, the delay² is of the order of ~ 67 ns. A second BPM at a zero-dispersion point with $\beta_{x,y} = 400$ m is used to detect pure betatron (orbit) errors: the delay in this

¹The FEXL can also be triggered by other machine protection signals, e.g. loss monitors.

²Assuming a cable signal velocity of $0.8c$

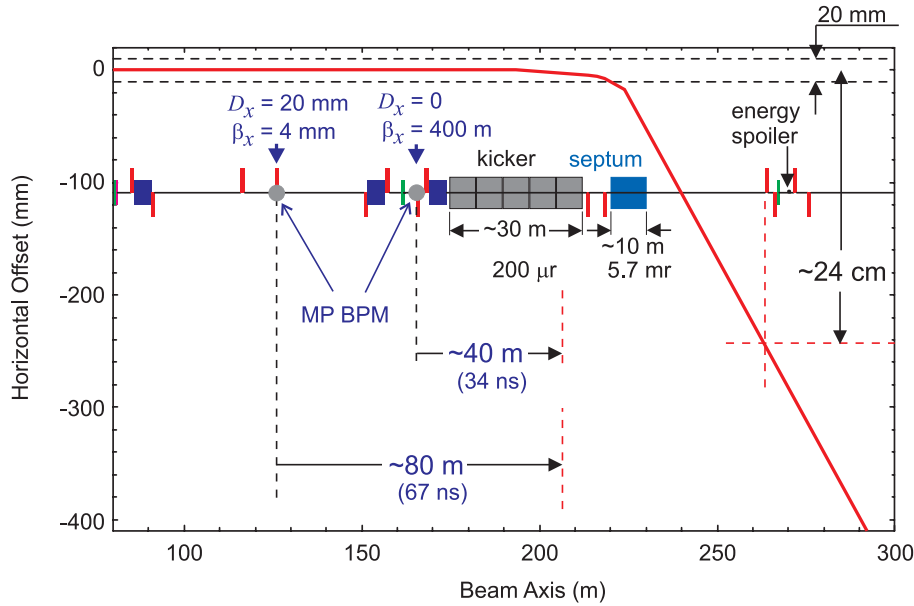


Figure 7.2.7: *Concept of the fast extraction (machine protection) system. Two machine protection (MP) BPMs are used to generate fast emergency signals, which can then be transmitted downstream to the fast kicker. Given the signal delay times, it is expected that (at the most) two bunches will be allowed through.*

case is ~ 34 ns. The kicker system comprises of 30×1 m kicker modules, giving a total kick of $\sim 200 \mu\text{r}$, with a rise time of 100 ns [9]. Allowing an additional 100 ns for signal processing, the total signal delay time is ~ 270 ns, which is still less than the bunch spacing of 337 ns. Hence only one (two at the most) bunches will be allowed through, before the remainder of the bunch train is safely extracted. When the FEXL is used as a commissioning line, two weak dipoles magnets are switched on to provide the same kick geometry as the kicker system.

The design of the lattice (including the septum magnet), is constrained by the following requirements:

- a -2% to -5% beam energy error¹ ;
- a possible failure of one kicker module (-3.5%);
- a kicker flat-top of $\pm 2\%$
- $\pm 0.5\%$ power-supply stability.

The beam is extracted horizontally, and then transported by a FODO system to a section comprising both a horizontal and vertical bend, which steer the beam down

¹Although positive energy errors $>2\%$ can occur under certain circumstances, they are considered far less likely than a negative energy error.

(~ 15 mrad) to the main dump. The optics is arranged to produce a beam size on the dump window that is larger than the required single pulse limit (see section 7.7).

A more detailed description of the FEXL system can be found in [10].

7.2.7 Magnet systems

Table 7.2.1 shows the basic magnet family types for the main BDS lattice. The magnets have been designed for cost-effective manufacture by:

- reducing the number of magnet families to a minimum; and
- restricting the power-supply requirements to those of standard commercially available supplies.

In particular, all dipole magnets are 1.8 m in length and have an aperture (vertical gap) of 20 mm: the long dipoles required in the arcs and CCS are then constructed from strings of these dipoles, allowing the necessary spacing for coils, vacuum pumps etc. Both an H-type and a C-type magnet have been designed.

Quadrupoles and higher-order multipoles are characterised by the standard apertures (diameters) of 20 mm, 40 mm and 140 mm. Figure 7.2.8 shows examples of cross-sections of some of the BDS magnets.

The total of 288 magnets in the main lattice are grouped into circuits where possible, resulting in 52 power-supplies, which themselves are grouped into three stability ratings (see 7.3). The magnets have power ratings ranging from 0.05–84 kW, with a more typical value of a few kW. The total power consumption for the main BDS lattice magnets is ~ 0.5 MW (one side).

Both the FEXL and the main extraction line contain strong dipoles (~ 1.4 T) which require a large amount of power. The power requirement for both extraction lines is $\sim 2 \times 1.5$ MW. The total power requirement for a single BDS (main lattice, FEXL and main extraction) is therefore ~ 4 MW, which includes ~ 0.5 MW for losses in power supplies, re-cooling etc.

Most of the power-supplies will be located in the tunnel close to the associated magnets to reduce cable lengths (costs). A redundancy system is foreseen where an emergency supply can be remotely ‘switched in’ should a supply in the tunnel fail, avoiding the need to access the tunnel directly. The failed supply can then be repaired during a routine scheduled maintenance break.

A complete description of all the BDS magnets, including detailed drawings and specifications, can be found in [11, 12, 13]. Details of the power supply system can be found in [28].

7.2.8 Vacuum system

The vacuum system is required to maintain an average pressure of 10^{-8} mbar (CO equivalent)¹. The vacuum chamber is constructed from stainless steel, which is copper

¹The pressure is calculated from limits on hard Coulomb gas scattering of the high-energy beam.

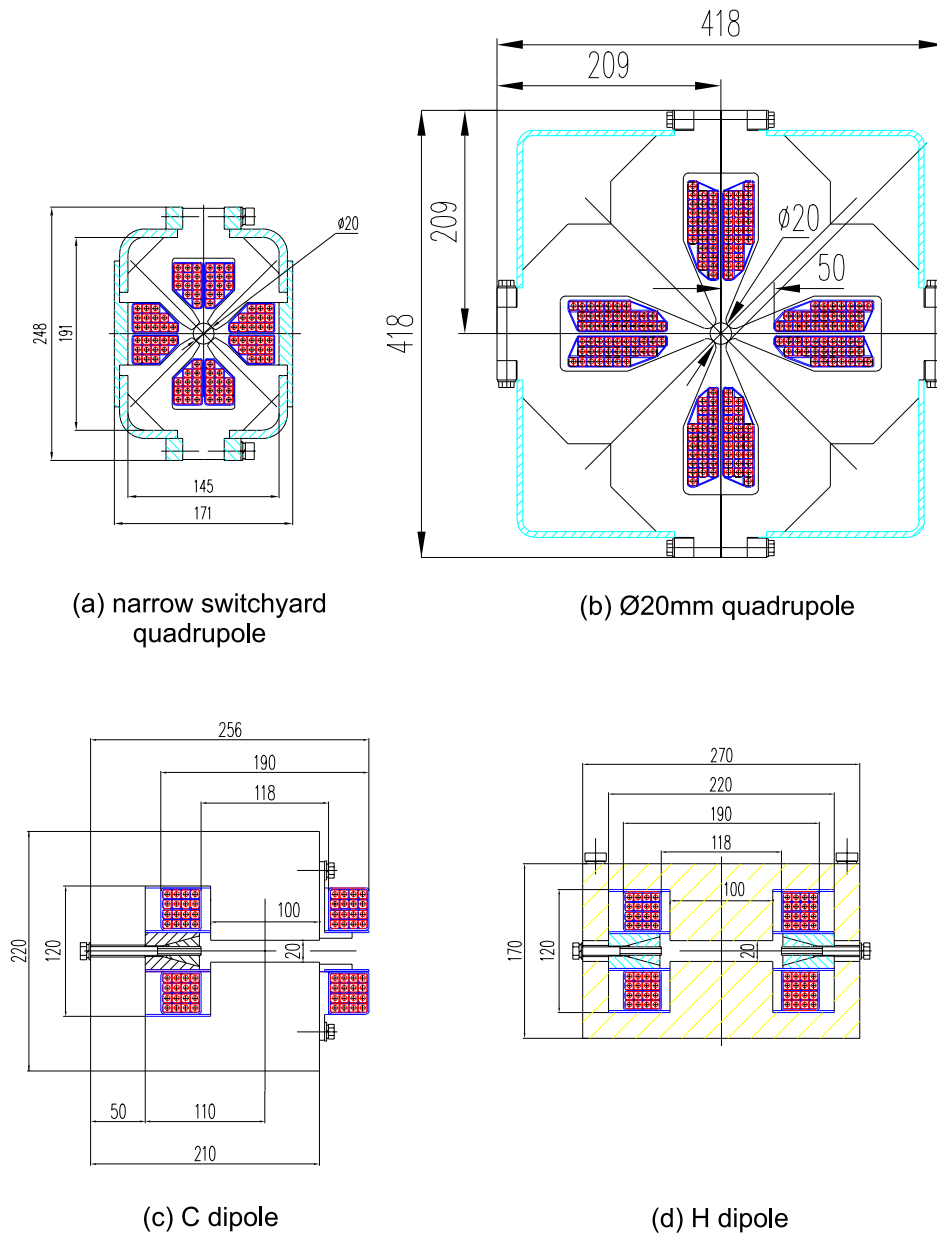


Figure 7.2.8: Cross-sections of four of the BDS magnets (taken from [11]): (a) Special narrow quadrupole used in the switchyard arcs (20 mm) (section 7.2.2); (b) standard 20 mm quadrupole; (c) C dipole (20 mm); (d) H dipole (20 mm). Dimensions are in mm.

<i>Magnet</i>	<i>Type</i>	<i>length</i> (<i>m</i>)	<i>Aperture</i> (<i>mm</i>)	<i>Field</i> (<i>Tesla</i>)	<i>No.</i>	<i>Total</i>
<i>dipoles</i>	H septum	1.8	20	0.12	24	185
	H (or C)	1.8	20	0.24	161	
<i>quadrupoles</i>	A	0.5	20	0.83	4	90
		1.0	20	1.14	48	
		1.5	20	1.14	16	
		2.0	20	1.02	14	
	B	1.5	20	0.79	4	
	C	0.5	40	0.72	2	
	D	2.0	140	0.75	2	
<i>sextupole</i>	E	0.5	20	0.26	2	12
		1.0	20	0.34	2	
		2.2	20	1.05	8	
<i>octupole</i>	F	0.5	20	0.29	1	1
					total:	288

Table 7.2.1: *Main magnets for a single BDS (not including extraction lines or the superconducting final doublet). Type refers to the magnet cross-section type; length to the core length; aperture is either the vertical gap height (dipoles), or the pole-tip diameter (quadrupoles, sextupoles and octupoles); field is the maximum pole-tip field for a beam energy of 400 GeV.*

coated on its inner surface to reduce the effects of resistive-wall wakefields on the beam. Ion getter pumps are used to maintain the vacuum. The design of the system is cost optimised by trading off the size of the pumps against the number required per meter of vacuum chamber. Because the magnets typically have small apertures (e.g. 20 mm diameter), the cross-section of the vacuum chamber is increased to 35 mm (where needed) to reduce the number of pumps; the transitions are tapered to reduce geometric wake effects. A total of ~ 380 pumps are required, with capacities of 21/s, 201/s, and 1251/s. Particular attention is paid to the region between the strong sextupole pairs in the HCCS and VCCS (section 7.2.5), where there is a tight tolerance on the allowed wakefield kicks: here the magnet aperture cross-section of 20 mm is maintained throughout the region to reduce geometric transitions. A complete detailed description of the vacuum system can be found in [14].

7.3 Luminosity Stabilisation

The combination of strong focusing and relatively large β -functions in the BDS result in some of the tightest alignment and field tolerances in the entire machine. There has been much work reported on the effects of ground motion and vibration in beam delivery

systems (for TESLA see for example [83, 15, 16]). In this section a comprehensive summary of the necessary stabilisation and tolerances for the TESLA BDS will be given. Due to the large aspect ratio $\sigma_x^*/\sigma_y^* = 550/5$, only effects in the vertical plane are generally considered.

When discussing luminosity stability, it is useful to separate out those losses due to beam-beam separation at the IP, and those due to an increase in beam size at the IP (bearing in mind that $L \propto 1/(\sigma_x^*\sigma_y^*)$). The mechanisms must then be further characterised by their time scales:

- those errors which occur on a time scale too fast to be actively compensated for (high frequency), or
- those which occur slowly enough to be corrected (low frequency).

For the case of ground motion and vibration, two correction (feedback) systems will be used:

- a fast (MHz) inter-bunch feedback system for correcting the beam-beam separation and collision angle at the IP;
- a slower (<0.1 Hz) orbit correction system for the entire BDS, which effectively keeps the beam centred in each magnet.

The IP inter-bunch feedback system (section 7.3.1) keeps the beams in collision. Since it works on a bunch-to-bunch time scale (337 ns), it effectively corrects all frequency components from d.c. to ~ 170 kHz. The slow orbit correction system (section 7.3.3) addresses slow ground motion drifts which perturb the orbit in the BDS, causing aberrations such as spurious dispersion to increase the beam size at the IP. Due to the 5 Hz repetition rate, the slow feedback can only be expected to correct frequencies below 1 Hz, and probably realistically only below ~ 0.1 Hz. The effects of aberrations caused by magnet vibration — and subsequent orbit motion — above ~ 1 Hz are currently not corrected for; these effects are summarised in section 7.3.2.

Section 7.3.4 briefly summarises the power supply tolerance (field stability) requirements. The final section (7.3.5) discusses luminosity tuning knobs, and requirements for beam-based alignment.

7.3.1 IP fast-feedback system

Due to the high vertical disruption parameter at the IP ($D_y \approx 25$), the luminosity is extremely sensitive to small offsets in both beam-beam displacement and crossing angle (see section 7.4). As a result, the collisions must be maintained to within $\sim 0.1\sigma$ in both offset and angle, or 0.5 nm and 1.2 μ rad respectively.

Figure 7.3.1 illustrates the concept for the IP beam separation feedback system. The large TESLA bunch spacing of 337 ns allows the use of a digital controller. Fast kickers (~ 100 ns) are used to make the necessary corrections. The feedback signal is

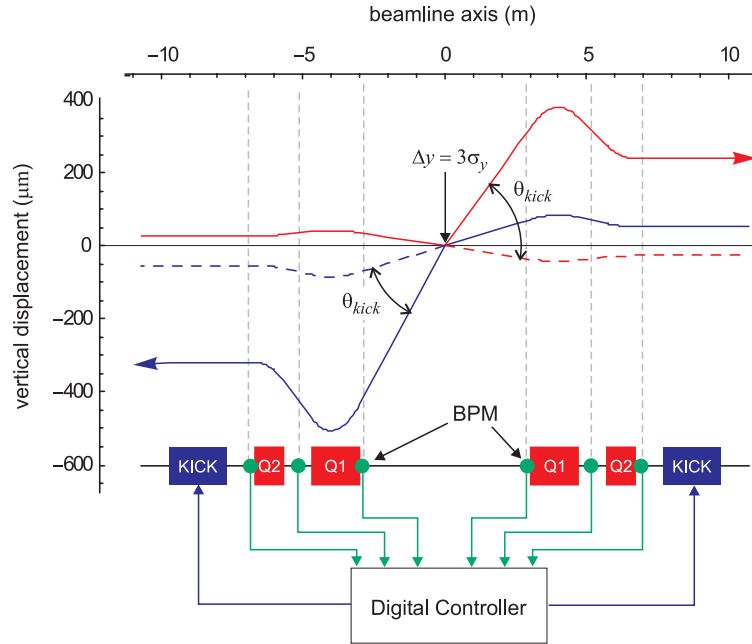


Figure 7.3.1: *The IP fast feedback system. The red and blue rays represent an example having a $3\sigma_y^*$ offset at the IP (corresponding approximately to a $10\sigma_y^*$ kick). The dotted lines represent the trajectories with no beam-beam kick. Initial (example) IP angles are 1 and $2\sigma_y^*$, for red and blue respectively.*

derived directly from the strong beam-beam kick which both beams experience when they do not collide head-on¹. Figure 7.3.2 shows the expected beam-beam kick versus beam separation for the design parameters. Since the feedback uses a linear algorithm, the slope of the beam-beam kick curve at $\Delta y = 0$ is used to calculate the offset; this approach has the advantage of making the feedback response as fast and accurate as possible for small beam-beam offsets, while having the disadvantage of a relatively long response time for larger offsets.

Two BPMs placed approximately 3 m away from the IP on either side are used to measure the beam-beam kick. Four more BPMs placed between and upstream of the final quadrupoles as shown in figure 7.3.1 can also be used. The BPMs need a spatial resolution of $5\ \mu\text{m}$ and a time resolution of 20 ns, the latter arising from the arrival time of the opposing bunch. For the primary BPMs (3 m), directionally coupled strip-line devices are currently considered, while for the other BPMs re-entrant cavities of the type currently used at TTF will be used [19] (see section 7.4.4 for more details on the IR region).

The fast kickers are based on an actual design currently being used in the TTF feedback test setup [20, 21]. They have a rise time of $\sim 100\ \text{ns}$ and a kick strength of $\sim 0.12\ \mu\text{r}/\text{m}$ (at 250 GeV). One-meter long kickers will be placed either side of the IR,

¹Such a feedback system based on the beam-beam kick was successfully used at the SLC [17].

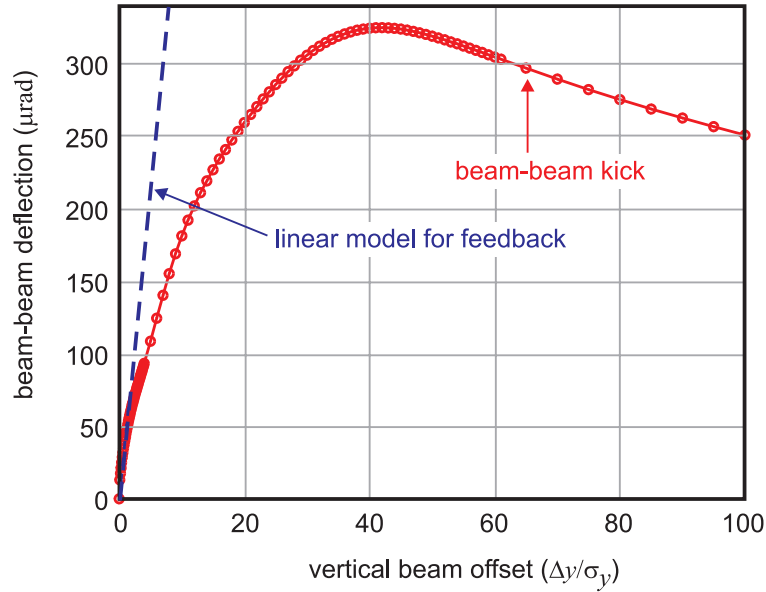


Figure 7.3.2: The beam-beam kick as a function of the relative offset for the nominal 250 GeV beam parameters (calculated using GUINEA-PIG[18]). The linear feedback model is also indicated.

which is sufficient to correct up to $\sim 100\sigma_y$ beam-beam separation: an RMS of $\sim 30\sigma_y$ is expected from calculations based on 70 nm RMS quadrupole vibration [16].

The time response of the feedback system is determined by the total delay time of the loop. The actual feedback algorithm currently favoured is a proportional-integral (PI) controller, giving a good d.c. rejection (step response) without compromising the high frequency attenuation. The current (simulated) system shows a damping of frequencies below ~ 170 kHz with approximately 15 dB per decade.

Figure 7.3.3(a) shows simulation results of the response to a $100\sigma_y$ step-function (including errors). The bunch train also contains the expected bunch-to-bunch offsets due to multi-bunch wakefield effects in the linac (see section 3.2). The initial offset is reduced by three orders of magnitude within ninety bunches, or 3% of the bunch train. After that, the bunches are controlled with the required $0.1\sigma_y$, corresponding to a luminosity loss of less than 10%.

Figure 7.3.3(b) shows the response of the angle feedback. To adjust the angle at the IP, a kicker must be placed at an IP image point upstream of the VCCS, so that the resulting kick is achromatic. An image-point in the β -matching section offers a relatively large β_y function (~ 52 m). Three one-meter kickers can correct $\sim 130 \mu\text{rad}$, or $\sim 10\sigma_{y'}$ at the IP. A BPM at a high β_y point in the VCCS (450 m downstream of the kicker) is used to correct any incoming vertical betatron oscillation. The resulting feedback delay is approximately $3.4 \mu\text{sec}$, or 10 bunches, which is still considered acceptable. In order to achieve the required resolution of $0.1\sigma_{y'}$, the signal BPM requires a spatial resolution of $1 \mu\text{m}$. Although the correction is effectively removed from the

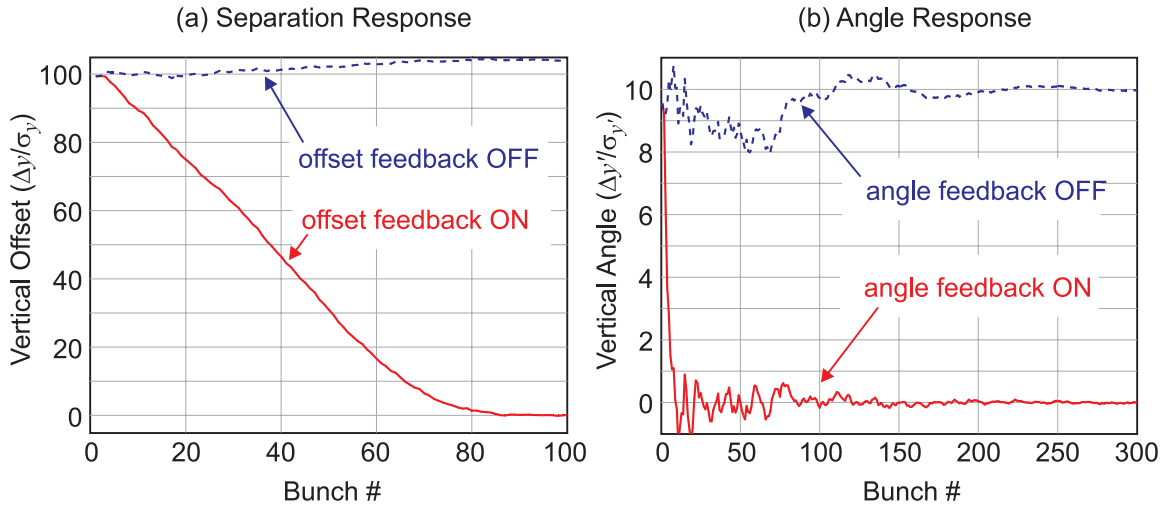


Figure 7.3.3: Results of simulations of the IP fast feedback for (a) a $100\sigma_y$ offset step function and (b) a $10\sigma_{y'}$ angle step function. Included in the simulation are: residual effects of multi-bunch wakefields in the linac; signal BPM noise of $5\mu\text{m}$ and $1\mu\text{m}$ for the position and angle respectively; 0.1% kicker field imperfections; a 10% random variation in the beam-beam kick.

IP, there is virtually no source of angle jitter downstream of the kicker in the FFS itself, since nearly all the magnets are $\pi/2$ out of phase with the IP [16].

Since the fast inter-bunch feedback system (section 7.3.1) is expected to correct the offset of each of the 5 Hz bunch trains independently, only the effects on the beam size (σ_y^*) will be considered in the following sections. Details of the fast IP feedback system can be found in [22].

7.3.2 Effects of fast quadrupole motion

In this section the effects of random uncorrelated quadrupole vibration on σ_y^* will be considered. Due to the 5 Hz repetition rate, these effects cannot be corrected. As a (pessimistic) reference, we will take an RMS quadrupole motion of 70 nm RMS, which corresponds to recent measurements at HERA ($f > 2$ Hz) [23]. A detailed account of the results presented here can be found in [16].

At any given instant, the magnets (quadrupoles) in the BDS will have random alignment errors due to vibration. The resulting kicks from these offset quadrupoles cause an ever increasing orbit amplitude in the downstream magnets. To estimate the effect on σ_y^* from the perturbed (vertical) orbit, the following aberrations must be considered:

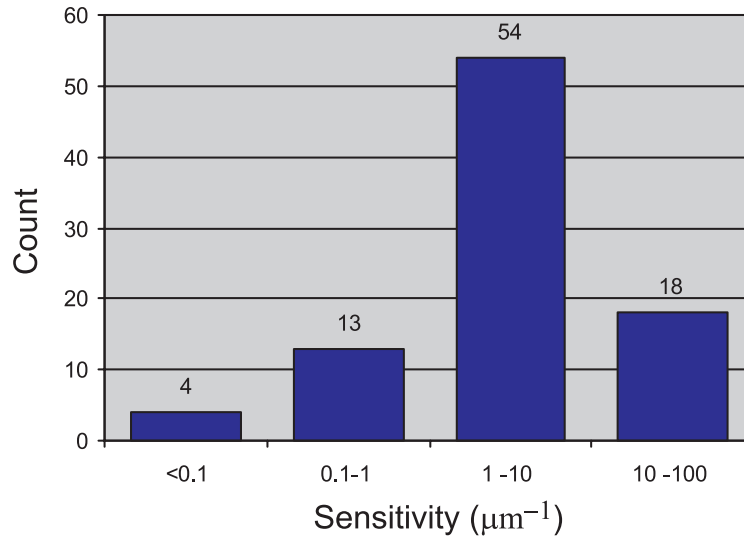


Figure 7.3.4: Summary of quadrupole sensitivity calculations. The sensitivity (μm^{-1}) is calculated as the inverse of the vertical quadrupole motion required to increase σ_y^* by 2%.

Aberration	contribution to $\Delta L/L$	comments
xy coupling	4.5%	both beams
linear dispersion	5.5%	e^- only
2 nd -order dispersion	2%	e^- only
total	12%	

Table 7.3.1: Summary of expected luminosity loss due to fast uncorrelated quadrupole motion (70 nm RMS). The loss is estimated only from an increase in σ_y^* (no beam-beam effects).

<i>magnet type</i>	<i>aberration</i>
quadrupole, sextupole	linear dispersion
quadrupole, sextupole	second-order dispersion
sextupole	xy coupling

In figure 7.3.4, the results of the vertical motion of single quadrupoles is summarised. The majority of the magnets have a sensitivity in the range of 1–10 μm^{-1} , corresponding to a $\Delta\sigma_y^*/\sigma_y^* = 2\%$ alignment tolerance of 100–1000 nm. 18 magnets have a tolerance < 100 nm.

Table 7.3.1 summarises the expected luminosity loss (no beam-beam effects) for 70 nm RMS quadrupole vibration. For the energy dependent terms (first- and second-order dispersion), only the contributions from the electron beam ($\sigma_{\Delta P/P} \approx 0.15\%$) to

the luminosity loss are considered, since the energy spread in the positron beam is much smaller ($<0.05\%$)¹

The total of 12% luminosity loss scales quadratically with the RMS vibration amplitude. Hence an amplitude of 35 nm would decrease the total to $\sim 3\%$. Should it be necessary, certain key quadrupoles can be actively stabilised to ~ 20 nm RMS using fast piezo-electric micro-movers [24].

7.3.3 Slow alignment drifts due to ground motion

Low-frequency motion (ground motion, $f < 1$ Hz) can be compensated using an orbit correction system (feedback), having a sample rate equal to the machine repetition rate of 5 Hz. For the current studies, the so-called ATL ground motion model has been used [25]:

$$\langle Y^2 \rangle = A \cdot T \cdot L$$

where Y is the relative offset of two points separated by a distance L after a time T . A is the constant of proportionality, and is generally quoted with the units $\mu\text{m}^2\text{m}^{-1}\text{s}^{-1}$. For the DESY site, a value of $A \approx 4 \times 10^{-6} \mu\text{m}^2\text{m}^{-1}\text{s}^{-1}$ has been measured [23], and this value will be assumed throughout the following section.

For the orbit correction, a simple one-to-one algorithm has been studied. An upstream corrector is used to steer the beam through the magnetic centre of the downstream magnet. For the simulations, it is assumed that

- each quadrupole has an additional horizontal and vertical dipole corrector associated with it;
- each magnet (quadrupole and sextupole) has an integrated BPM with a given resolution (noise);
- the BPM offsets with respect to the (magnetic) centre of the associated magnets have been accurately determined using beam-based alignment techniques;
- systematic residual BPM offsets are assumed to be zero.

The last item requires some clarification: after applying beam-based alignment techniques, there will be some finite residual BPM offsets. These offsets are considered to be static, and so their effects on the luminosity can be initially ‘tuned out’ using the tuning knobs described in section 7.3.5. To study the effects of *random* BPM noise, we set the *static* offsets to zero.

Figure 7.3.5 shows the results of simulating 1000 pulses at 5 Hz. The plot clearly shows the trade-off between random BPM noise and the feedback time constant¹. As

¹the electron energy spread comes from the undulator for the positron source (see 4.3).

¹the feedback time constant is adjusted using a ‘gain’ factor ($0 < g < 1$) which defines how much of the calculated correction should be applied per 5 Hz pulse. A gain of 1 (100% correction) corresponds to a time constant of 0.2 s, while a gain of 0.1 corresponds to 2 s.

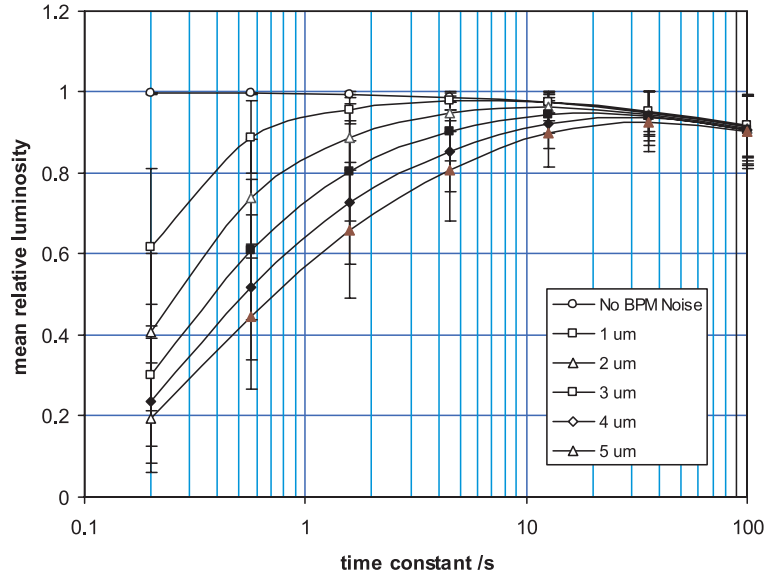


Figure 7.3.5: Results of simulations of the effect of ATL-like ground motion on luminosity, as a function of the orbit correction feedback time constant and RMS BPM noise. Each point represents the average over 1000 simulated pulses (200 seconds).

the time constant is increased, the BPM noise is effectively integrated away. Above $\tau \approx 20$ s, all the curves come together, and the effects of the ground motion itself begin to dominate. Assuming that we will have a BPM resolution of $1\mu\text{m}$, a time constant of ~ 8 s would seem to give the minimum luminosity loss ($\sim 2\%$).

Figure 7.3.6 shows the results of simulating the effects of ground motion over a longer time scale (~ 10 days). Since the time steps taken represent many 5 Hz pulses, the orbit corrections are applied ‘one-shot’ with a gain of 1. No BPM noise is included in the simulation. The results are plotted for three different cases:

1. no correction — shows the effects of ground motion on the luminosity if no correction is applied. The luminosity rapidly drops to zero as the beams move out of collision.
2. IP fast feedback on — shows the results with the fast feedback on, effectively keeping the beams in collision (section 7.3.1). The luminosity stability is increased by more than two orders of magnitude, but still falls off due to aberrations generated by the orbit in the BDS.
3. both IP feedback and orbit correction on — represents the full stabilisation of the BDS. The luminosity is now constant and only begins to slowly fall off after several days.

The drop in luminosity for the fully corrected case is a direct result of the one-to-one steering algorithm: such algorithms are not ‘dispersion free’, and eventually the

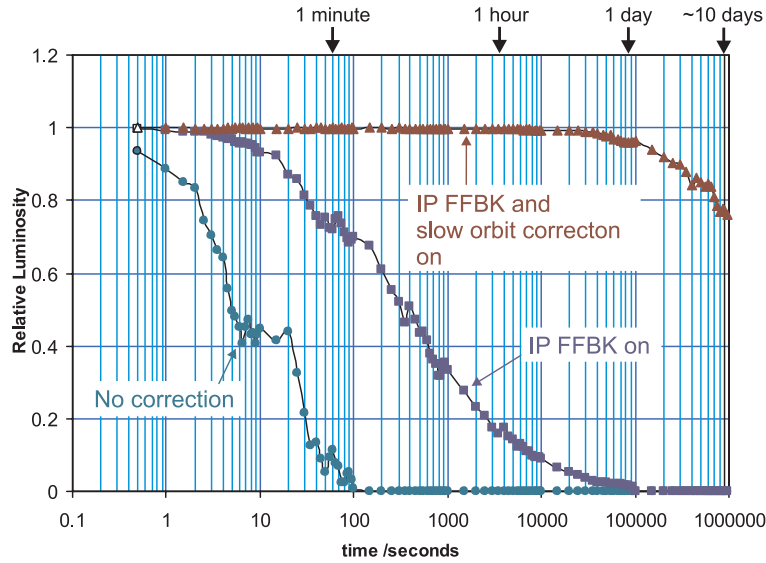


Figure 7.3.6: *Luminosity loss due to ATL-like ground motion as a function of time. Each curve represents an average over 20 random seeds of simulated ground motion (see text for more details).*

residual dispersion generated by the corrector kicks will begin to degrade the luminosity. A dispersion-free steering algorithm would certainly result in longer time stability. On the time scale of days, however, it is a relatively simple task to re-tune the IP dispersion using a dispersion tuning knob (section 7.3.5). For more details of the simulations see [16].

Note: the results shown in figures 7.3.5 and 7.3.6 were based on an electron energy spread of 0.18%. As of writing, a re-design of the positron undulator (section 4.3) has now reduced the estimated energy spread to $\sim 0.15\%$. Since the luminosity loss $\Delta L/L \propto (\Delta P/P)^2$, this will reduce the effects by $\sim 30\%$.

7.3.4 Power supply tolerance requirements

Where possible, the magnets are placed in series and connected to a single power supply, resulting in a total 52 power supplies for a single BDS. The power supplies are divided into three stability groups: 10^{-4} , 5×10^{-5} and 10^{-5} . The requirements are summarised in table 7.3.2. The partition of the tolerance budget was made to minimise the number of high-stability supplies, while keeping the total expected luminosity loss to less than 3%. All supplies can be obtained commercially to the required specification [28].

7.3.5 Initial luminosity tuning

In order to achieve the design luminosity, it will be necessary to perform two initial tuning steps:

Stability	Num. of PS	Num. of Magnets	Comments
10^{-4}	41	80	
5×10^{-5}	6	28	MES bend string CDS quad* CCS quad* weak FT doublet
10^{-5}	5	178	s.c. final doublet, CCS bend strings, ARC bend strings
totals	52	286	

* *specific quadrupoles only*

Table 7.3.2: Summary of power supply stability requirements. The total luminosity loss from the specified tolerances is $\sim 3\%$ (taken from [16]).

beam-based alignment of the type successfully used at the FFTB [26] will be initially required to (a) align the magnets to within some accuracy over a long baseline, and (b) to accurately determine the BPM offsets;

orthogonal IP tuning is used to tune out the effects of residual (static) BPM offsets and magnet alignment after beam-based alignment.

Due to ground motion and vibration effects, it will be necessary to re-apply the orthogonal tuning at specific time intervals (~ 10 days, see 7.3.3). Eventually it may even be necessary to repeat the beam-based alignment procedure, although current simulation results suggest that this is unlikely within a typical luminosity run period (~ 5000 hours).

For the IP tuning, five orthogonal optics knobs are required:

- x - and y -waist
- x - and y -dispersion
- x - y coupling

The above knobs can be constructed by moving the strong sextupole pairs in the two CCS sections. By selecting various combinations of horizontal or vertical, symmetric or anti-symmetric motion of a specific sextupole pair, all five required aberrations can be cleanly generated (corrected) at the IP. Table 7.3.3 summarises the motions required. It is currently foreseen to place all eight CCS sextupoles on mechanical movers. The movers will have a resolution (step size) of $\sim 1 \mu\text{m}$ and a range of $\pm 1 \text{mm}$. Three of the combinations listed for the VCCS pairs have 2% limits below $1 \mu\text{m}$: it is probably

Aberration		Sextupole pair	Motion Type	3β Range (μm)	2% limit (μm)
waist	x	HCCS		52	7
		VCCS	horizontal	413	58
	y	HCCS	symmetric	346	48
		VCCS		3.6	0.5
dispersion	x	HCCS	horizontal	121	18
		VCCS	anti-symmetric	465	70
	y	HCCS	vertical	19	2.6
		VCCS	anti-symmetric	2.6	0.4
coupling		HCCS	vertical	7.4	1
		VCCS	symmetric	2.1	0.3

Table 7.3.3: Summary of the various CCS sextupole mover combinations and their effects. The 3β range is the typical scan range required, while the 2% limit gives that motion needed to reduce the luminosity by 2% (taken from [27]).

therefore better to only use the less sensitive HCCS sextupole pairs to provide the required knobs.

Beam-based alignment has been successfully demonstrated in several machines, and particularly at the FFTB [26], where quadrupole alignment errors of $50\ \mu\text{m}$ to below $1\ \mu\text{m}$ were achieved. In [27] an estimate of the required precision of initial alignment was made, based on the maximum allowed residual second-order dispersion generated after alignment and one-to-one steering¹. The precision varies depending on the ‘wavelength’ or baseline length over which the alignment is to be applied. For the current BDS, the alignment requirements range from $<20\ \mu\text{m}$ RMS over short distances ($<10\text{m}$) up to $\sim 80\ \mu\text{m}$ RMS over longer baselines ($\sim 500\text{m}$). While short magnet-to-magnet alignment tolerances on the order of $10\text{-}20\ \mu\text{m}$ should be achievable with the methods used at the FFTB, the longer baseline tolerance may well prove difficult: second-order dispersion knobs, or better steering and tuning algorithms will probably be required.

7.4 Interaction Region and Beam-Beam Effects

The beam-beam interaction at the IP of a linear collider will be very intense. To minimise the effects, flat beams with large aspect ratios $R = \sigma_x^*/\sigma_y^*$ are used at the IP, resulting in a strong beam disruption only in the vertical plane. Disruption is quantified by the *disruption parameter*, D_y , defined as the ratio of the bunch length σ_z to the vertical beam-beam focal length f_y :

$$D_y \equiv \frac{\sigma_z}{f_y} = \frac{2r_e N_b \sigma_z}{\gamma \sigma_x^* (\sigma_x^* + \sigma_y^*)}$$

¹the tolerance is based on a 2% increase in σ_y^* due to the residual second-order dispersion.

cm energy	[GeV]	$\sqrt{s} = 2E_0$	500	800
Luminosity	$[10^{34}\text{cm}^{-2}\text{s}^{-1}]$	L	3.4	5.8
Bunch population	$[10^{10}]$	N_b	2	1.4
Transverse bunch sizes	[nm]	σ_x^*, σ_y^*	553, 5	391, 2.8
Transverse bunch divergences	$[\mu\text{rad}]$	Θ_x^*, Θ_y^*	37, 12	26, 7
Bunch length	[mm]	σ_z	300	300
Disruption parameters		D_x, D_y	0.22, 25	0.20, 27
Upsilon parameter		Υ	0.06	0.09
Average relative energy loss		δ_B	3.2	4.3
Number of photons/ e^\pm		n_γ	1.6	1.5
Spent beam power	[MW]	P_{SB}	11	17
Beamstrahlung photon power	[kW]	P_γ	360	760
Number of pair particles		N_P	129 000	153 000
Average pair particle energy	[GeV]	$\langle E_P \rangle$	2.8	5.3

Table 7.4.1: TESLA IP Parameters.

where N_b is the bunch population. The relatively high TESLA value of $D_y \approx 25$ indicates that particles undergo several vertical oscillations while crossing the opposing bunch. *Beamstrahlung* (i.e. the emission of synchrotron radiation in the coherent e.m. field of the opposing bunch) is also considerable at these high beam energies. It is usually characterised by the *Upsilon* parameter:

$$\Upsilon \equiv \frac{2 \langle E_c \rangle}{3 E_0} = \frac{5 r_e^2 \gamma N_b}{6 \alpha_e \sigma_z (\sigma_x^* + \sigma_y^*)}$$

where $\langle E_c \rangle$ and E_0 are the average photon critical energy and the beam energy respectively. With a photon yield of about $1.6/e^\pm$, beamstrahlung causes a significant energy loss in the spent beam, resulting in a 3–4% average energy loss characterised by a long tail. The associated luminosity spectrum $d\mathcal{L}/d\sqrt{s}$ is also degraded (see section 7.4.1). A small fraction of the beamstrahlung photons are converted into low energy e^+e^- pairs which form the most numerous background source to the detector. On the positive side, the pair flux is proportional to the luminosity and can therefore be used to monitor relative luminosity variations on a bunch to bunch basis[30, 31].

Beam-beam effects are analysed in more detail in [29]. They influence the collider performance in essentially three ways described in the following sections.

7.4.1 Luminosity enhancement and luminosity spectrum

Results of beam-beam simulations using GUINEA-PIG [18] show that the mutual focusing of the bunches at the IP leads to a luminosity enhancement factor of ~ 2 with respect to the geometric luminosity. Figure 7.4.1 shows (a) the luminosity as a function of the longitudinal position of the vertical waist, and (b) the corresponding number of pairs striking a forward detector at a radius of $r > 12$ mm. The luminosity is maximum

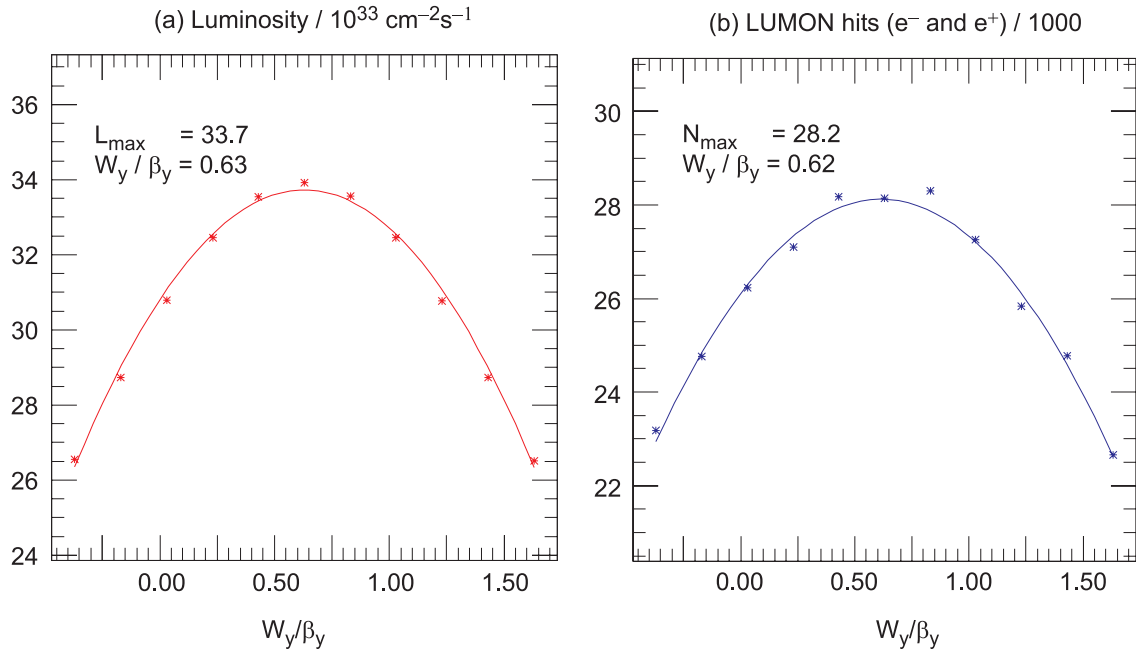


Figure 7.4.1: *Luminosity optimisation relative to the longitudinal position of the vertical waist for TESLA 500 GeV c.m. energy. (a) shows the actual luminosity as a function of waist position (relative to the IP, $W_y/\beta_y = 0$), while (b) shows the numbers of e^+e^- pairs detected in the fast luminosity monitor. Solid lines show the parabolic fits through the 11 data points.*

when the bunches are focused to vertical waists located about $0.63 \times \beta_y^* \simeq 250 \mu\text{m}$ in front of the IP. Figure 7.4.1(b) shows that the detected pairs can be used to achieve the optimum (maximum) luminosity. The gain from the luminosity enhancement is somewhat offset by the dilution due to beamstrahlung of the luminosity spectrum $d\mathcal{L}/d\sqrt{s}$ towards lower centre of mass energies (figure 7.4.2). However, about 60% of the total luminosity is still produced at energies higher than 99.5% of the nominal c.m. energy.

7.4.2 Sensitivity to vertical displacements and angles

The high disruption regime ($D_y \approx 25$) results in a high sensitivity of the luminosity to both vertical beam-beam offset and crossing angle. The luminosity loss for offset and angle errors is shown in figure 7.4.3, where simulation results[18] are compared to the analytic expressions without beam-beam forces. The sensitivity is enhanced by a factor of five for small offsets, and by a factor of ten for small angles with respect to the simple geometric factor. The aggressive optimisation of the IP parameters into this high disruptive regime is justified by the use of the fast inter-bunch orbit feedback system (section 7.3.1), which will be capable of maintaining the beams in collision to within the specified tolerances.

Given the extreme sensitivity to offset and angle, some loss of luminosity is also

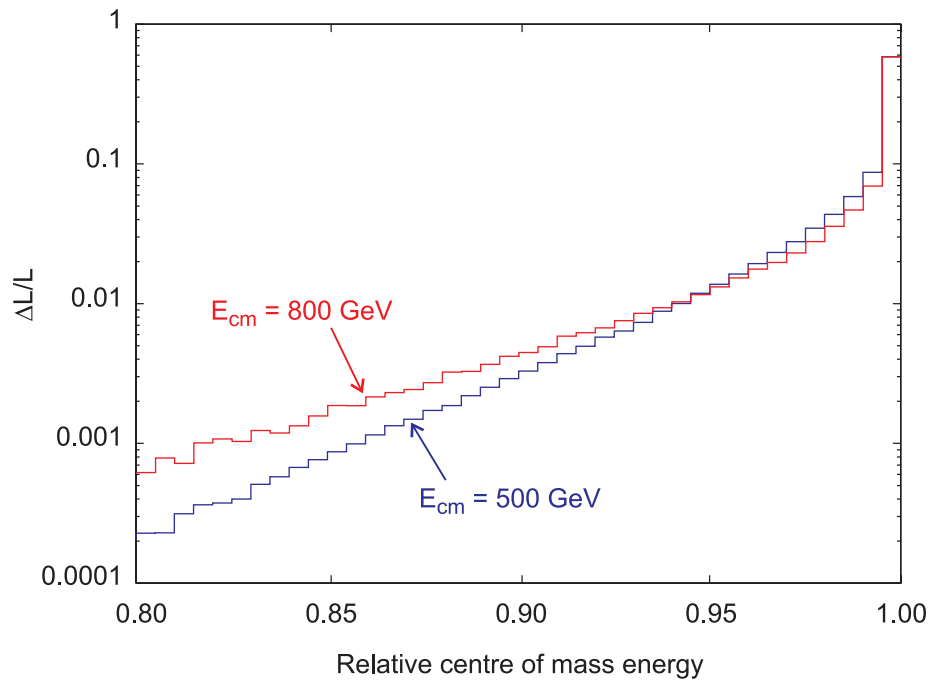


Figure 7.4.2: *Luminosity spectra for 500 GeV and 800 GeV centre of mass energy.*

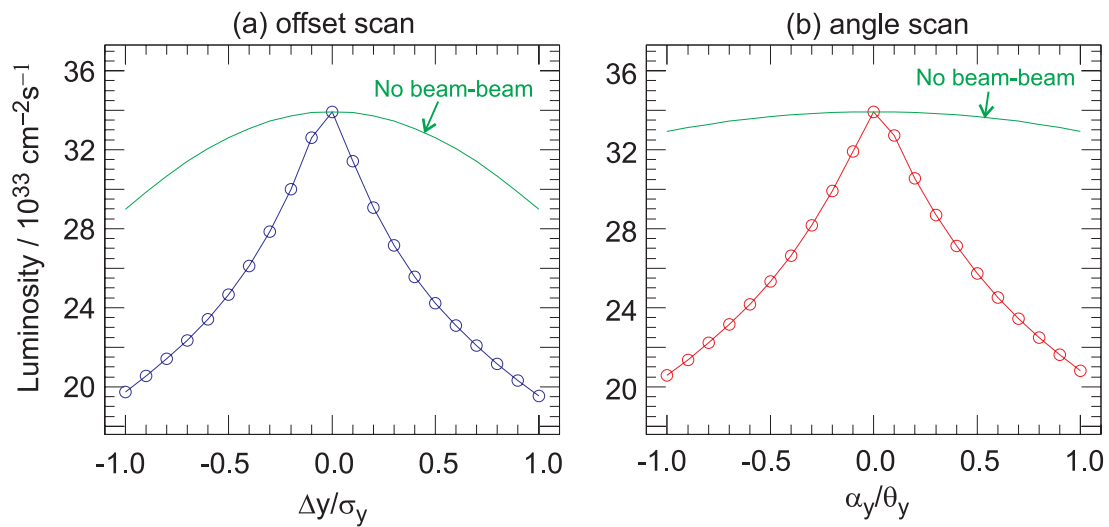


Figure 7.4.3: *Luminosity loss as a function of normalised IP vertical offset and angle for TESLA 500 GeV.*

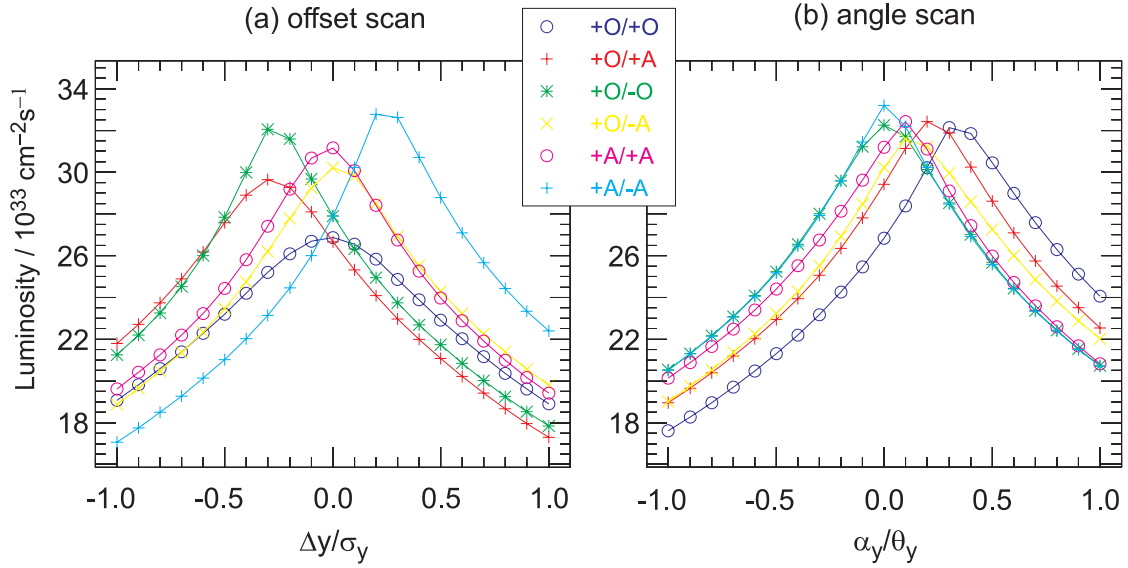


Figure 7.4.4: (a) Offset followed by (b) angle scans of the luminosity for various combinations of vertical to longitudinal correlations leading to 6% e^\pm correlated emittance growth. $\pm O$ = offset (y -plane) correlated, $\pm A$ = angle (y' -plane) correlated

expected from internal bunch deformations, such as those induced by single-bunch wakefields in the linac (the so-called ‘banana effect’). The single-bunch *correlated* emittance growth from wakefields is expected to be 6% on average (see section 3.2). Figure 7.4.4 plots the luminosity obtained from colliding electron and positron bunches with a 6% correlated emittance growth. The bunches are initially generated with the correlated emittance growth either entirely in the displacement (y) plane or in the angle (y') plane, including all six sign combinations. In all cases, the nominal luminosity can almost be recovered by optimisation of the beam offset (figure 7.4.4(a)) followed by an angle scan (figure 7.4.4(b)). The optimum set point can be found by monitoring the luminosity on a bunch to bunch basis using the pair signal. The impact of beam-beam instability is discussed in more detail in [32].

7.4.3 Beam-beam backgrounds

The charged particle beam-beam background is essentially the result of three basic processes:

1. beamstrahlung emission — the energy-degraded spent beam dominates the spectrum of charged particles above 100 GeV;
2. pair creation — e^+e^- pair particles dominate the spectrum below 20 GeV;
3. Radiative Bhabhas or (beam-beam) bremsstrahlung — this incoherent process creates same sign e^+ or e^- particles moving along with the beam.

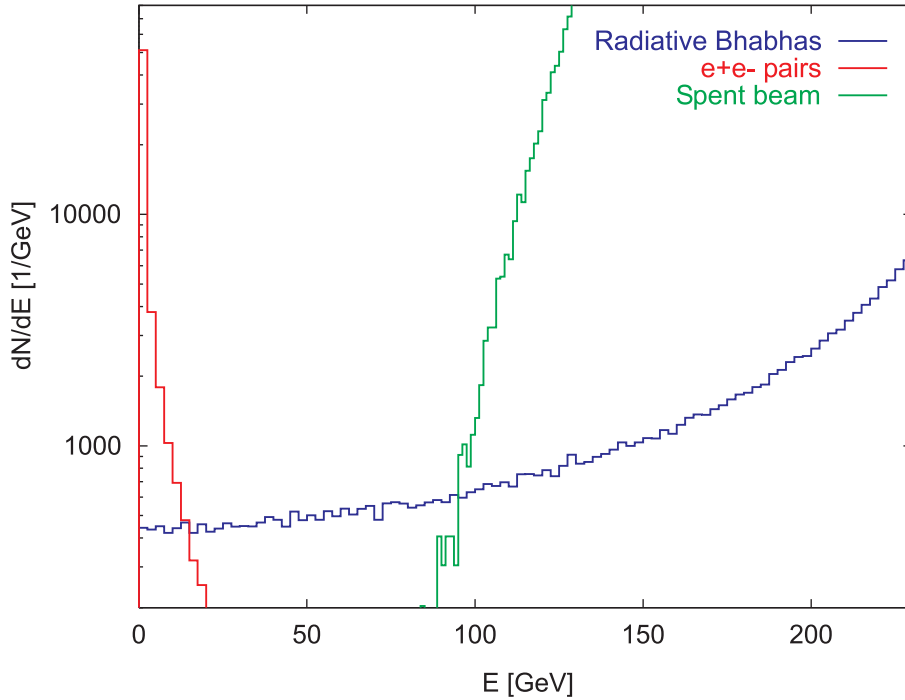


Figure 7.4.5: *Energy spectrum of charged particle backgrounds for 500 GeV c.m. energy.*

The various energy spectra are plotted in figure 7.4.5 for 500 GeV c.m. energy. The rate of radiative Bhabha in the intermediate energy range around 50 GeV provides a signal proportional to luminosity which — although less powerful than the pair signal — can also be used for machine tuning [30]. In addition, beamstrahlung photons carrying 3–4% of the beam power are emitted in a narrow forward cone of about ± 0.15 mrad. The extraction and disposal of these background sources is discussed in section 7.7; their impact on the detector is discussed in Part IV chapter 6 of this report.

7.4.4 Interaction region (IR) and last doublet design

The layout of the IR is shown in figure 7.4.6. The most important regions are:

- the instrumented mask constructed from high Z material to absorb most of the e^+e^- pairs and their secondaries; and
- the cryostat housing the final super-conducting quadrupole doublet.

In the beam direction, the aperture limitations are set by the forward cylindrical mask of 24 mm diameter housing the pair luminosity monitor, and by the super-conducting quadrupole doublet itself, consisting of a 1.7 m and a 1.0 m long quadrupole ($dB_y/dx = 250$ T/m), with an inner diameter of 48 mm. A schematic cross-section of the doublet is shown in figure 7.4.7, and a detailed design is described in [33].

Figure 7.4.6 also shows the instrumentation required for beam tuning:

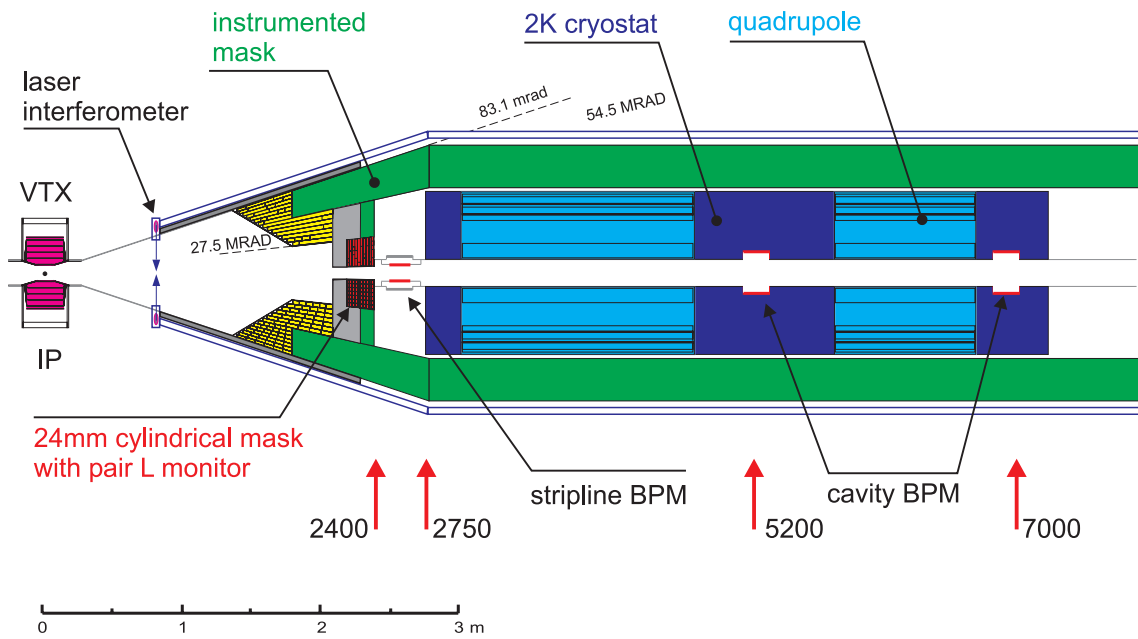


Figure 7.4.6: Interaction region layout.

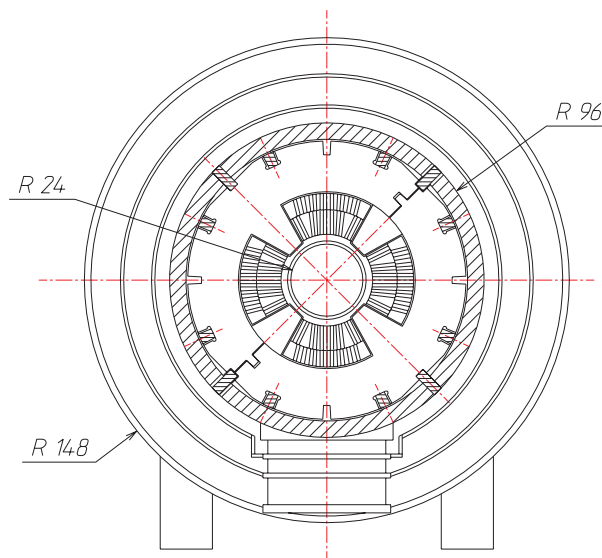


Figure 7.4.7: Cross-section of the super-conducting final doublet quadrupole and cryostat.

- one stripline and two cavity beam position monitors (BPM), which are primarily used by the inter-bunch fast feedback system (section 7.3.1);
- a laser interferometer [34] for single beam profile measurement at 0.8 m from the IP;
- one luminosity monitor (pair counter) on each side of the IP located at the lowest aperture radius of 1.2 cm on the inner mask;

Finally, a slower luminosity monitor, integrating the bremsstrahlung signal over about 10 bunch crossings, is foreseen around the beam pipe at 8.5 m from the IP (not shown).

7.5 Collimation System

The collimation system uses thin mechanical spoilers followed by thick absorbers to physically scrap the halo particles off the beam. The design of the optics are constrained by:

- the required physical aperture for the given collimation depth;
- spoiler survival considerations in the event of a direct hit from the beam;
- wakefield effects from the narrow aperture of the spoiler jaws.

Since it is the spoilers which effectively define the collimation aperture, we will interchangeably use the word collimator and spoiler in the following sections. The absorbers are large blocks of material (~ 20 radiation lengths), which sit in the geometric shadow of the spoilers. The exact (most efficient) location of the absorbers is still to be determined. For the spoilers, we assume that one radiation length of titanium will be used.

The following sections give a concise synopses of the current status of the collimation system. More detailed information can be found in [3].

7.5.1 Required collimation depth

Halo particles with large amplitudes will radiate photons in the quadrupoles close to the IR; in particular, photons generated within the strong final doublet may strike inner parts of the detector and cause unacceptable background. The required collimation depth is defined as the aperture within which photons generated by halo particles pass cleanly through the IR. Figure 7.5.1 shows the limiting case for photons generated by an incoming halo in the final doublet; the resulting collimation depth is $\pm 13\sigma_x$ and $\pm 80\sigma_y$, where $\sigma_{x,y}$ are the nominal transverse beam dimensions at 250 GeV [35].

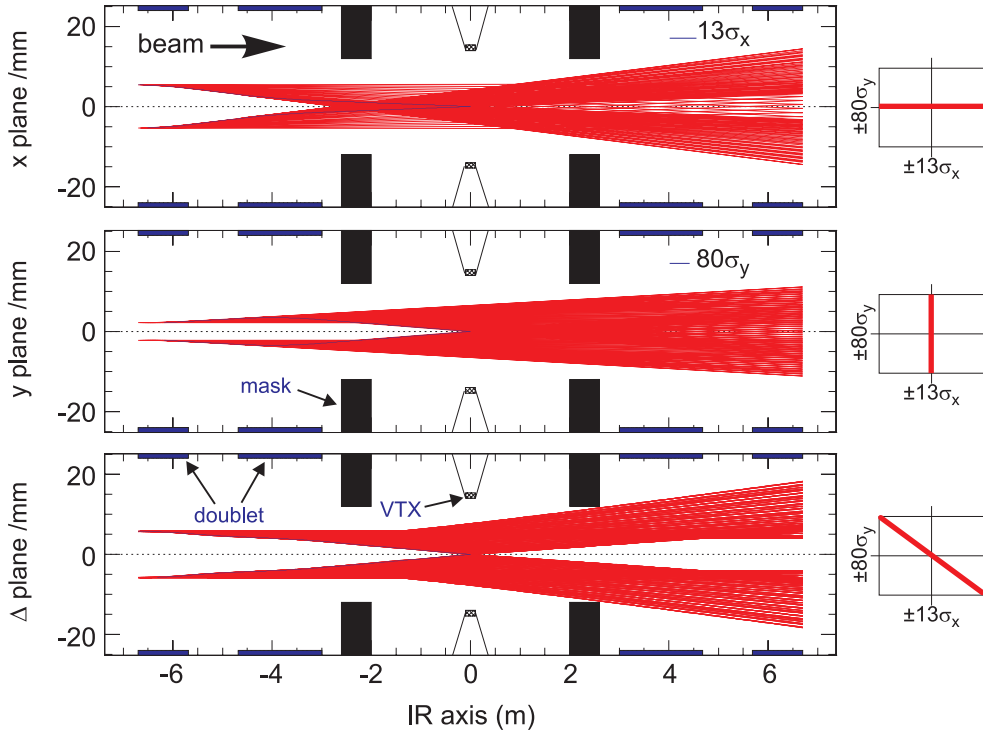


Figure 7.5.1: *Synchrotron radiation fan generated by the last quadrupoles and traced through the IR. The envelope defines the required collimation depth of $\pm 13\sigma_x$ and $\pm 80\sigma_y$. The limiting aperture is defined in the diagonal (Δ) plane by the exit 24 mm mask (see section 7.4.4 for more details of the IR region).*

7.5.2 Optics

The main (primary) collimation section consists of a series of five identical cells, with $\beta_x = \beta_y = 800\text{ m}$ at the symmetry points where the spoilers are located. The phase advance per cell (spoiler) is effectively 45° in both planes¹. Figure 7.5.2 shows the optics. The first spoiler is at a high dispersion point ($D_x = -100\text{ mm}$), and is used as the momentum collimator. The remaining four spoilers are located in a zero dispersion region, and are referred to as the betatron collimation system; they effectively define an octagon in phase space as depicted in figure 7.5.2. The physical apertures of the spoilers are set to a factor $\cos(45^\circ/2) \approx 0.92$ smaller than the required collimation depth, which fits the octagon defined by the spoilers inside the ellipse defined by the collimation depth. A second set of spoilers are located at the high β -points in the HCCS and VCCS; these collimators are positioned at the sine-like phase with respect to the IP, and so directly shadow the final doublet aperture. They are set to collimate exactly at $\pm 13\sigma_x$ and $\pm 80\sigma_y$. The physical apertures of all the spoilers are listed in table 7.5.1.

The values in table 7.5.1 represent the phase space acceptance for a linear system

¹due to optics constraints, the actual phase advance is $\phi_x = 45^\circ$ and $\phi_y = 315^\circ$.

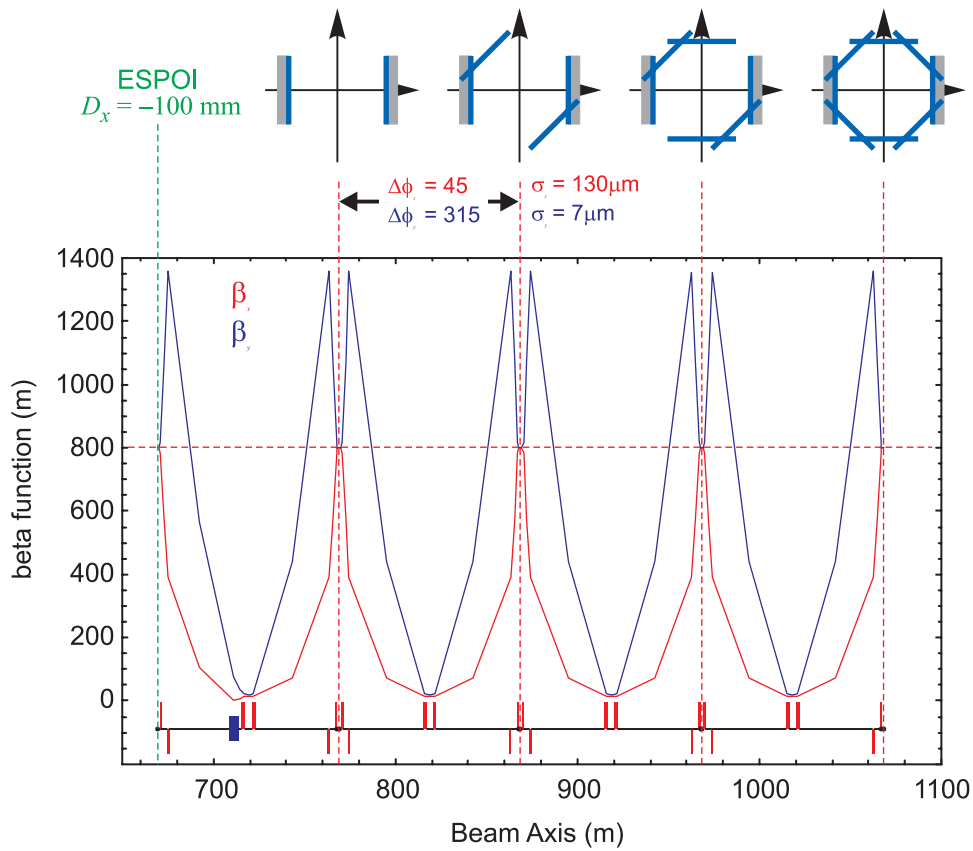


Figure 7.5.2: The primary collimation and diagnostics system (CDS).

Spoiler	Aperture		Acceptance		
	x/mm	y/mm	$\pm x/\sigma_x$	$\pm y/\sigma_y$	$\pm\Delta P/P$ (%)
ESPOI	3	-	12	-	1.5
XSPOI	3	1	12	74	-
COLX	3.9	0.6	13	80	5.7
COLY	0.9	2.7	13	80	2.9

Table 7.5.1: Physical apertures (gaps) and the linear acceptance of the various spoilers in the BDS. ESPOI = energy spoiler, XSPOI = betatron spoilers (CDS), COLX(Y) = CCS spoilers.

only: the relatively strong chromaticity of the lattice and the non-linear elements in the MES (section 7.5.3) cause off-momentum particles to be driven to large (betatron) amplitudes. Particle tracking was performed to check that the system collimates correctly. All physical apertures were treated as ‘hard’ edges (i.e. no scattering). Figure 7.5.3 summarise the results of tracking 10^5 particles; figure 7.5.3(b) shows that there are no particles remaining outside of the required collimation aperture at the entrance to the final doublet.

7.5.3 Spoiler protection

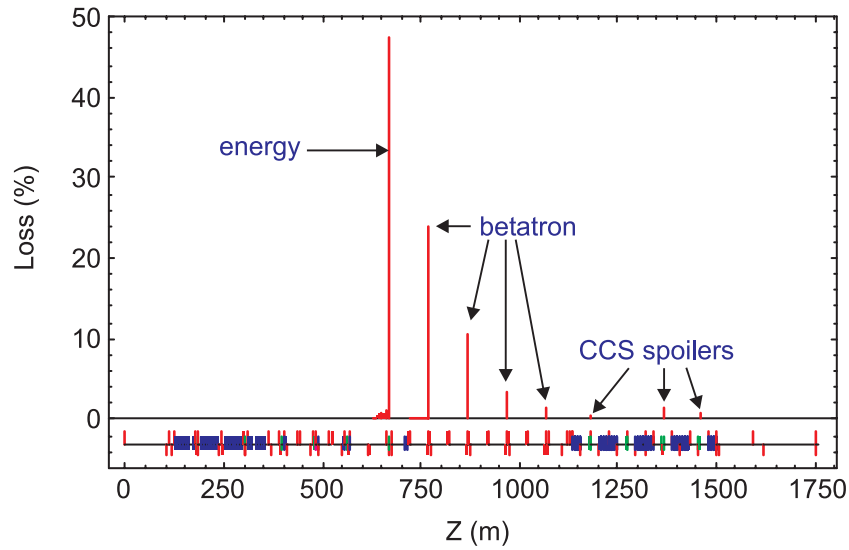
The spoilers are by design the limiting apertures in the machine: when a bunch train comes out of the linac with a large orbit or energy error, it is the spoilers that should intercept the beam first. In the event of some upstream error, the fast emergency extraction line (FEXL, section 7.2.6) should safely extract the beam after one or two bunches: hence the spoilers need only survive at most two bunches from the bunch train.

The current spoiler design uses one radiation length of titanium (3.56 cm). Studies using GEANT4 [3] have shown that the spoiler should withstand a single *design* bunch ($128 \times 7\mu\text{m}^2$) with some safety margin. The calculation uses the ultimate tensile strength (σ_{UTS}) as the survival criterion for the spoiler [83, 3, 36]. However, recent experiments using the SLAC linac have indicated that failure tends to occur at lower instantaneous power densities than the GEANT studies would suggest [37], and so an additional level of protection seems prudent.

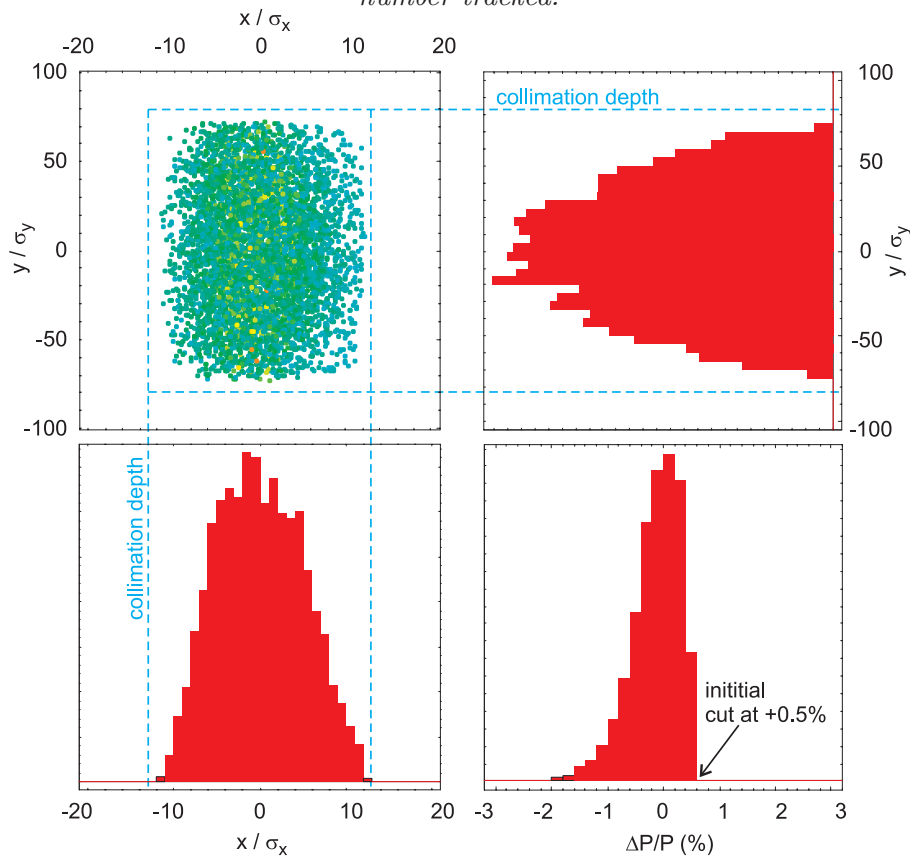
The original collimation system reported in [83, 36] reflected the philosophy that *all* spoilers should be able to survive a direct hit from some number of bunches. The beam size at each spoiler was blown up using linear optics to reduce the peak energy particle density to an acceptable level. The system was characterised by large (km) β -functions, resulting in relatively long systems with extremely tight tolerances. Such systems eventually proved to be impractical and have been abandoned. The current philosophy is to protect the spoilers from energy errors, since these are the most likely (frequent) type of error we can expect from the linac. Large orbit (pure betatron) oscillations of sufficient amplitude to strike a spoiler are probably rare events by comparison: the typical scenarios tend to be magnet failures, which occur relatively slowly ($> 100\mu\text{sec}$), and can be detected by direct monitoring.

A non-linear magnet system referred to as the magnetic energy spoiler (MES) is incorporated just upstream of the collimation system. Figure 7.5.4 indicates how the system works. An off-momentum bunch receives a horizontal kick from the octupole at the high dispersion point ($D_x = -100\text{mm}$), which translates into a (momentum dependent) horizontal offset at the downstream skew-sextupole¹. The effective *skew-quadrupole* generated couples the horizontal emittance into the vertical plane. The result is a significant increase in the vertical beam size at the energy collimator, placed $(n + 1/2)\pi$ downstream in both x - and y -phase. From a simple thin-lens analysis, the

¹the octupole effectively generates third-order dispersion at the skew-sextupole.



(a) Particles 'losses' along the beamline, expressed as a percentage of the initial particle number tracked.



(b) Particle distribution at the entrance to the final doublet after tracking through the entire BDS.

Figure 7.5.3: Results of particle tracking through the BDS. All apertures are treated as 'hard' edges, i.e. a particle outside of a given aperture is deemed lost. An initial flat distribution of 10^5 particles was generated, with a transverse extent of $\pm 16.25\sigma_x$ and $\pm 100\sigma_y$ (collimation depth plus 25%). The momentum distribution was $-3\% < \Delta P/P < +0.5\%$. Effects of scattering and transmission through material are not included.

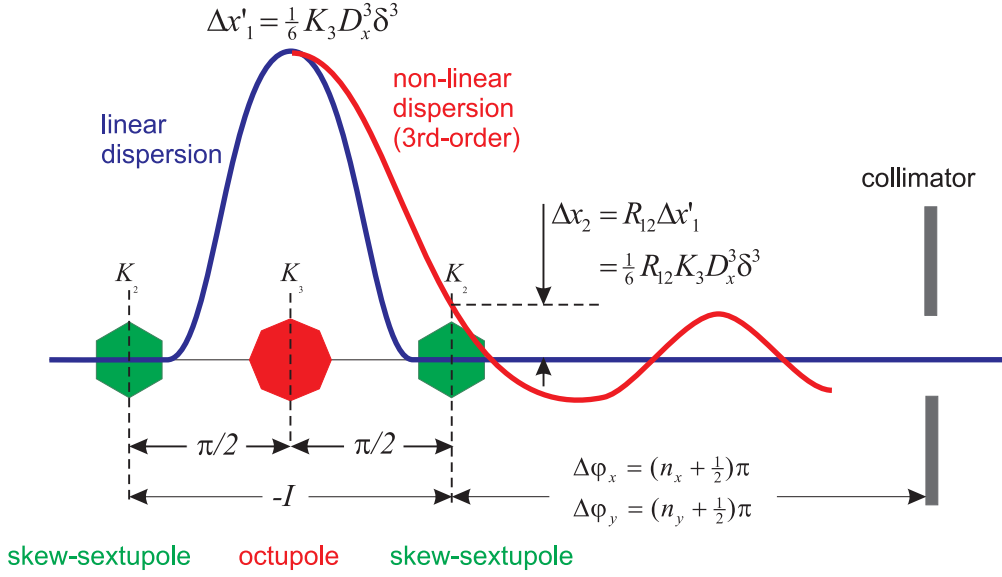


Figure 7.5.4: Concept of the magnetic energy spoiler (MES). See text for details.

increase in vertical beam size at the spoiler as a function of momentum error $\delta = \Delta p/p$ is

$$\frac{\sigma_y(\delta)}{\sigma_y(\delta = 0)} \approx \frac{1}{6} K_2 K_3 R_{12} \sqrt{\beta_x \beta_y} \sqrt{\frac{\epsilon_x}{\epsilon_y}} D_x^3 \delta^3$$

where K_2 , K_3 are the integrated strengths of the skew-sextupoles and octupole respectively, D_x is the linear dispersion at the octupole, R_{12} is the linear Green function from the octupole to the skew-sextupole, and $\beta_{x,y}$ are the β -functions at the skew-sextupole. The system also generates centroid kicks to the beam, resulting in third-order horizontal dispersion and sixth-order vertical dispersion. These energy dependent orbits eventually cause the beam to strike a betatron collimator in CDS section. If the collimator apertures are set at $\pm N_x \sigma_x$ and $\pm N_y \sigma_y$, the maximum relative increase in beam size, defined at the point when the beam hits a betatron spoiler, is given by

$$\left. \frac{\sigma_y(\delta)}{\sigma_y(0)} \right|_{max} \approx 2 \frac{N_y}{N_x}$$

For the current system, the limit corresponds to $2 \times (80/13) \approx 12$. However, chromatic effects in the downstream CDS lattice that are not included in the above analysis constrain the maximum obtainable factor still further. The current values of $K_2 = 5 \text{ m}^{-2}$ and $K_3 = 640 \text{ m}^{-3}$ are set to give a factor of ~ 6 increase in vertical beam size, which has been confirmed using tracking (see figure 7.5.5).

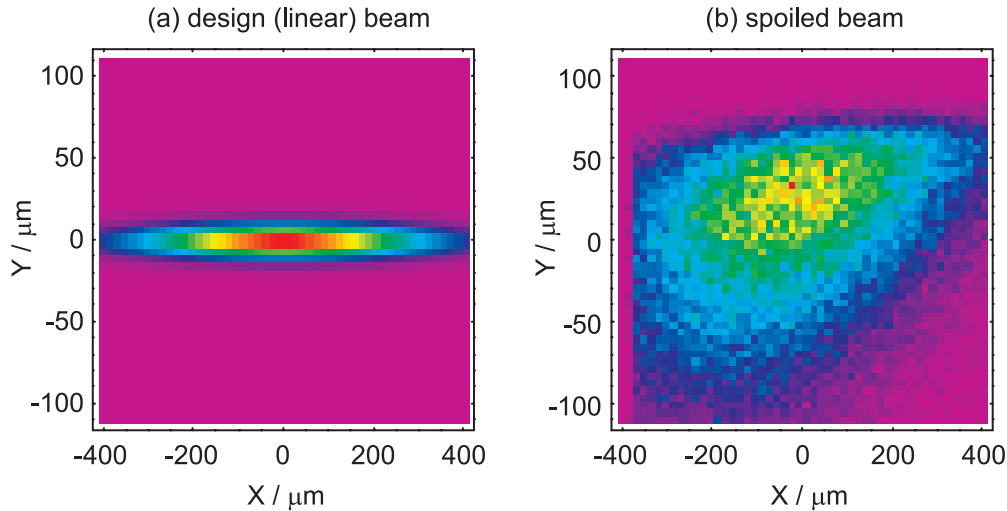


Figure 7.5.5: Results of tracking a design beam with a momentum centroid error of $\Delta P/P = -2\%$. (a) shows the design beam on the energy spoiler (ESPOI), while (b) shows the results of the tracking. The beam area is increased by a factor of 6.

7.5.4 Wakefield considerations

For one radiation length of titanium at the specified apertures, the resistive wall wakefield can be ignored. To reduce the geometric wakefield to an acceptable level, the spoilers will be constructed with tapers approximately 1 m long. Simple estimates based on calculations presented in [36] suggest that vertical beam offsets on the order of a few σ_y cause less than a 2% emittance growth. In addition, recent experimental results from SLAC [38] have shown that such theoretical estimates are pessimistic by as much as a factor of ten. Even with the conservative theoretical estimates, however, there appears to be no significant wakefield effects.

7.6 Beam Extraction

After collision at the IP, the highly disrupted beams must be cleanly extracted from the IR and transported without significant losses to the main dump. In addition, the intense beamstrahlung generated during the beam-beam interaction must be cleanly extracted and dumped. A third requirement is to safely transport the undisrupted charged particle beams to the main dump in the event that there is no collision (i.e. no beam-beam interaction); in this case, the optics of the extraction line must generate a large enough beam size on the dump window to prevent single pulse damage. The various extracted beam parameters are summarised in table 7.6.1. A detailed description of the extraction system design can be found in [39].

With the exception of the energy spread for the undisrupted beam case (see table 7.6.1), the extraction systems are identical and symmetric about the IP. Unless

		Spent e^\pm	Beamstrahlung	Undisrupted e^\pm	
$E_{cm} = 500$ GeV					
Av. Power	[MW]	P	10.9	0.360	11.3
Av. Energy	[GeV]	$\langle E \rangle$	242	5.1	250
Divergence	[μ r]	$\Theta_{x,y}$	245, 27	151, 36	37, 12
Emittance	[10^{-12} m]	$\epsilon_{x,y}$	67, 0.18	–	20, 0.061
Energy Spread	[%]	σ_E/E	5.5	–	0.15(e^-)/0.032(e^+)
$E_{cm} = 800$ GeV					
Av. Power	[MW]	P	16.8	0.760	17.5
Av. Energy	[GeV]	$\langle E \rangle$	283	11.4	400
Divergence	[μ r]	$\Theta_{x,y}$	152, 17	94, 21	26, 6.8
Emittance	[10^{-12} m]	$\epsilon_{x,y}$	28, 0.68	–	10, 0.019
Energy Spread	[%]	σ_E/E	7.4	–	0.15(e^-)/0.032(e^+)

Table 7.6.1: *Main characteristics of the disrupted spent beams, beamstrahlung photons and undisrupted (low emittance) beams at the IP.*

explicitly stated, the following description applies to both e^+ and e^- systems.

7.6.1 Electron and positron beam extraction

The charged beam extraction line (figure 7.6.1) is based on the following concepts:

- The beams are transported to water dump systems (section 7.7) located 240 m downstream of the IP.
- The beams are *vertically* extracted outside of the IR (i.e. outside of the final s.c. quadrupoles) and before the first parasitic bunch crossing¹.
- 20 m of electrostatic separators (ESEP1 and ESEP2) provide an initial separation of incoming and outgoing (extracted) beams, with an angle of 0.8 mrad. The separators have both a d.c. electrostatic and magnetic deflectors combined in the same unit; the electric and magnetic deflections add up for the outgoing beam while they cancel each other for the incoming one.
- A total downward angle of 15 mrad is primarily achieved by a magnetic septum MSEP and the dipoles BV1 and BV2; the angle is constrained by the need to minimise the muon rate at the surface.

¹The first parasitic bunch crossing is at 50 m and 26 m for 500 GeV and 800 GeV c.m. energy respectively.

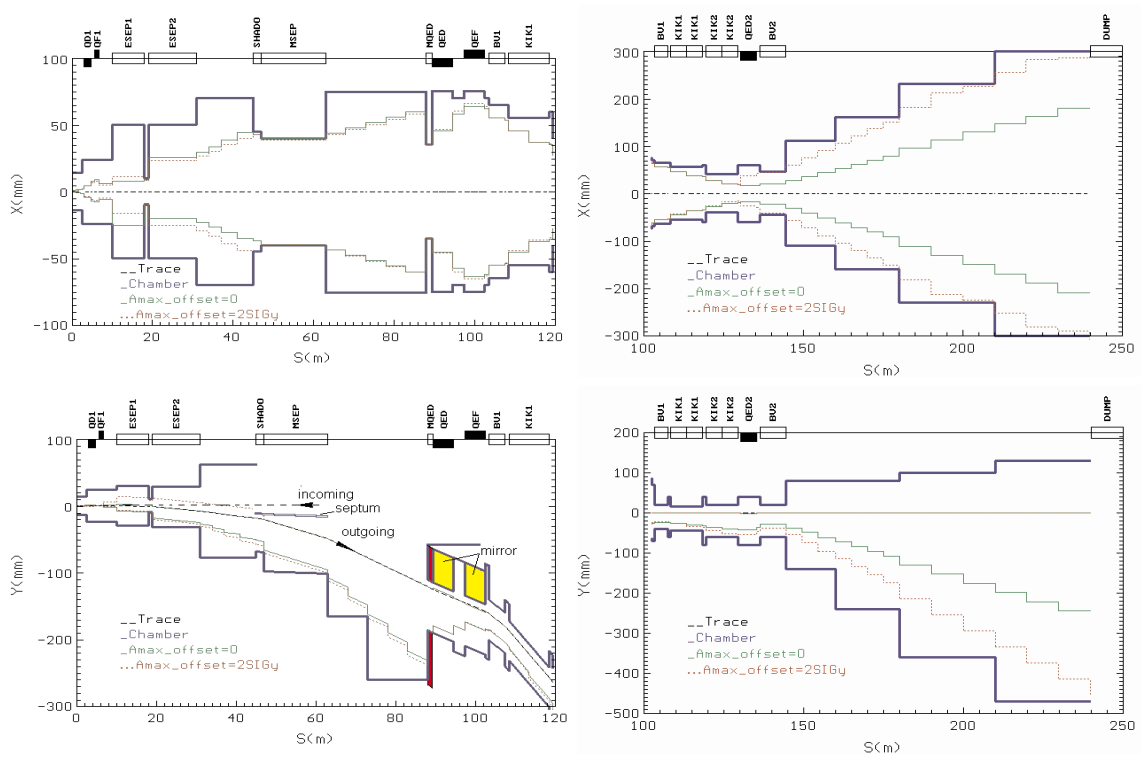


Figure 7.6.1: *Horizontal (top row) and vertical (bottom row) layouts and beam pipe apertures of extraction beam line.*

- The beam optics shown in figure 7.6.2 is designed to limit the disrupted beam losses to less than 0.1% along the beam line. This is done by controlling the vertical dispersion generated by the extraction bends with a proper arrangement of septum quadrupoles (QED, QEF, and QED2) with magnetic mirror blades. About 0.01% of beam power is lost at the collimator embedded in the separator and at the magnetic-septum shadow (SHADO), and 0.1% at the quadrupole collimator (MQED).
- The same optics blows up the spot size of the undisrupted (low emittance) beams above 0.4 mm^2 at the dump window (see figure 7.6.3). To increase the effective beam size still further, two 10 m long fast-sweeping magnets (KIK1, KIK2) sweep the bunch train in a circle of 5 cm radius; the water temperature rise is then limited to 40° C (see section 7.7).

The electrostatic separators are constructed from $5 \times 4 \text{ m}$ units based on the design used in LEP [40], where they have reached the 50 kV/cm field needed for the 500 GeV c.m. energy machine. For the upgrade to $E_{cm} = 800 \text{ GeV}$, either the field or the length or both need to be increased: while a field of 80 kV/cm is feasible, it has yet to be

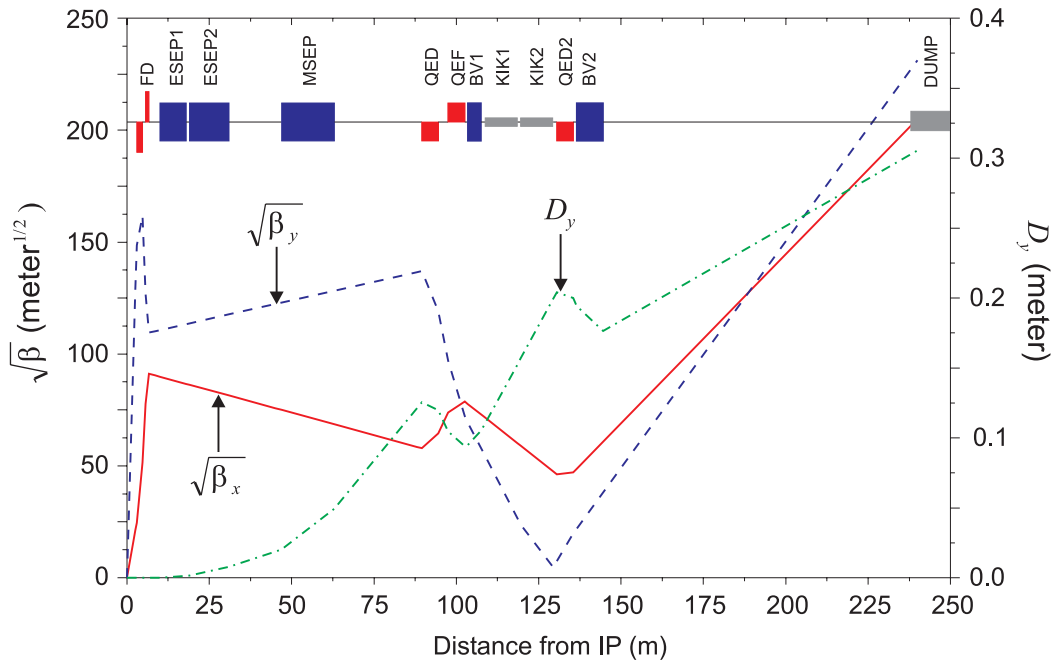


Figure 7.6.2: Optics of the charges particle extraction line.

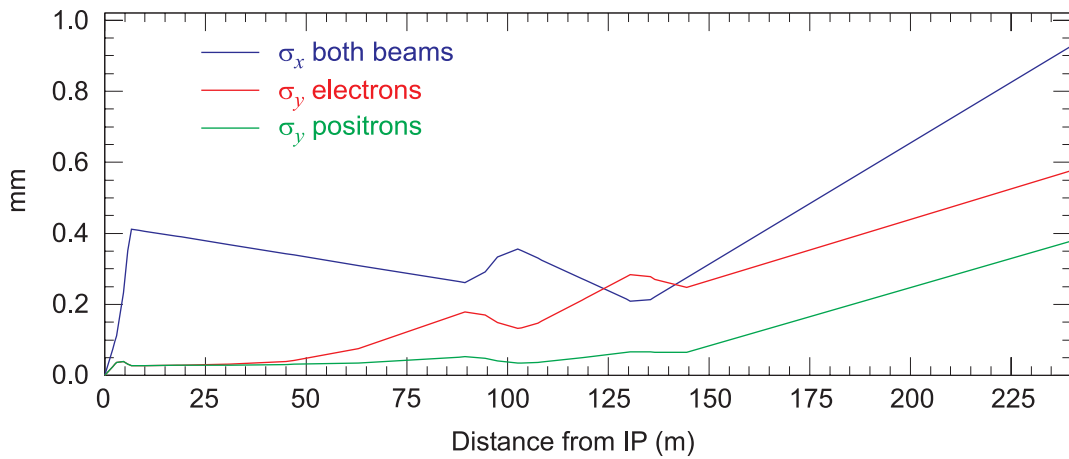


Figure 7.6.3: Beam sizes of the undisrupted (low emittance) electron and positron beams along the extraction line. The blow-up of the vertical emittances due to synchrotron radiation in the vertical bends is also included.

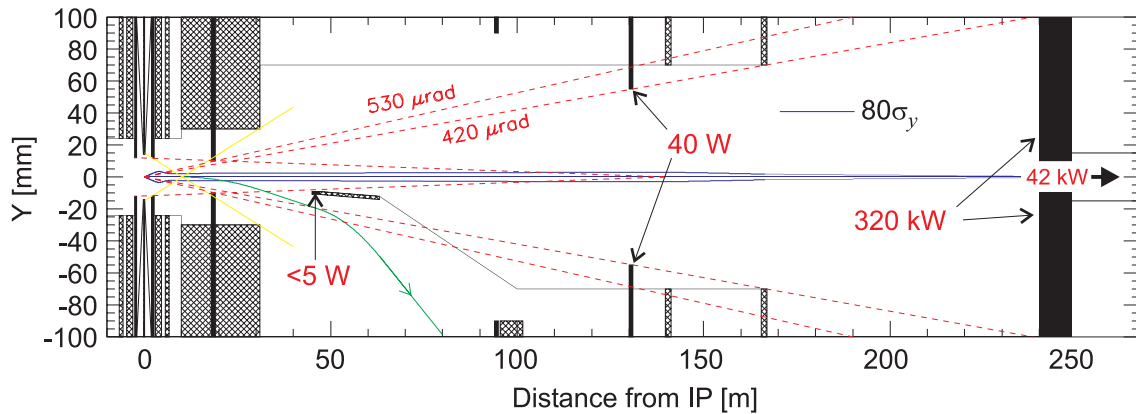


Figure 7.6.4: Vertical layout of the final transformer region. The beamstrahlung power levels on the collimators are for the $E_{cm} = 500$ GeV machine.

demonstrated and requires further R&D. The field of the 16 m long vertical septum magnet is kept low (~ 0.1 Tesla) to allow for a thin septum blade of a few millimetres; a complete description can be found in [13].

7.6.2 Beamstrahlung photon extraction

The 360 kW of beamstrahlung power is extracted cleanly through the large aperture final telescope to a water dump. To localise the main power deposition in one heavily shielded area, the beamstrahlung dump is located (integrated) at the same position as the main spent beam water dump (240 m downstream of the IP)¹. The key features of the system (shown in figure 7.6.4) are:

- a 10 mm radius collimator located 18 m from the IP (designed to mask the detector from the incoming synchrotron radiation) intercepts less than 1 W of beamstrahlung power;
- the intermediate quadrupole doublet (~ 150 m from the IP) with 70 mm bore radius is shielded by a 55 mm radius collimator which intercepts about 40 W of beamstrahlung power;
- the main beamstrahlung collimator (dump), which has a central 20 mm diameter aperture to allow for the incoming beam; the ~ 40 kW of low-angle beamstrahlung which passes through this aperture is dumped in a smaller (solid) beam dump located directly after the first C-dipole of the CCS.

¹This results in the stretching of the final telescope optics discussed in section 7.2.5.

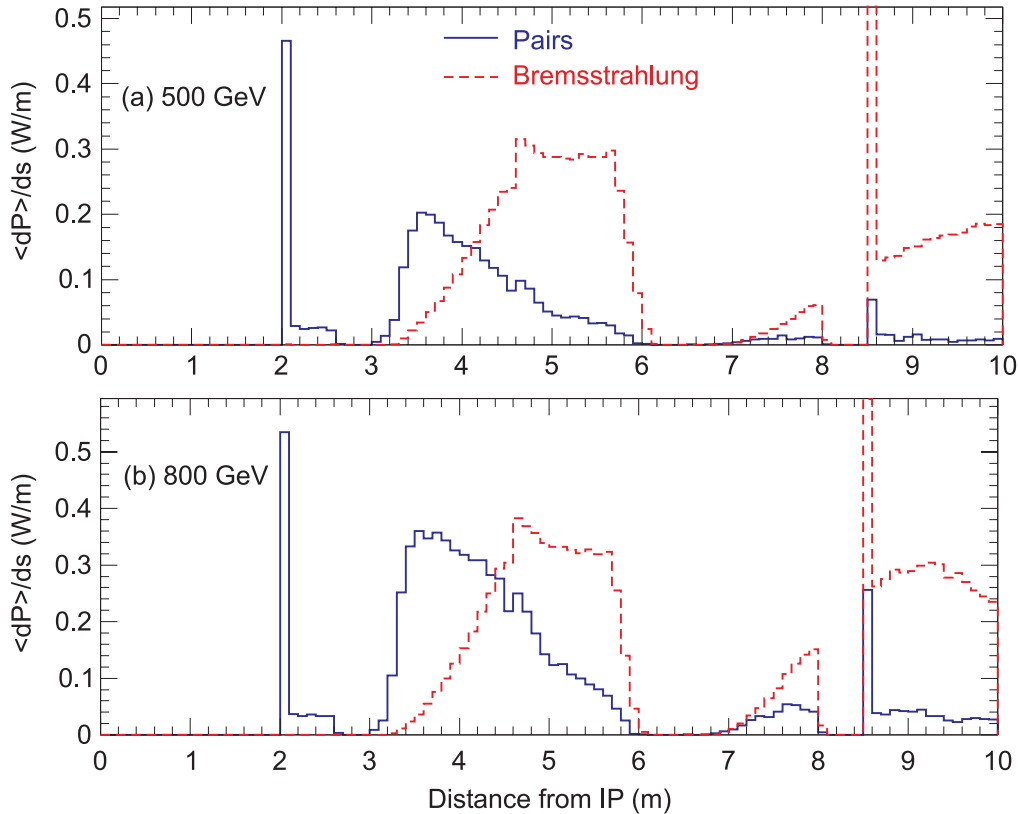


Figure 7.6.5: Average power density (W/m) deposited by the e^+e^- pairs and the radiative Bhabhas (bremsstrahlung) in the IR.

7.6.3 Pairs and radiative Bhabhas power deposition

Although the ± 10 m region around the IP is free from spent beam loss, lower energy radiative Bhabhas and e^+e^- pairs — which experience large disruption during the bunch collision — are over-focused by the IR doublet quadrupoles. The power densities deposited on the beam pipe (shown in figure 7.6.5) are smaller than the 3 W/m limit set by cooling capacity of the cryogenic system for the s.c. IR quadrupoles [33].

7.7 Main Beam Dump System

This section discusses the main characteristics, features and safety aspects of the main beam dump system. Many of the basic considerations of the dump system are discussed in detail in [83]: in the following, therefore, emphasis is placed on those aspects that differ or are new. A more detailed description of certain subcomponents of the system can be obtained from the cited references. The numbers quoted are for the design beam power for the 500 GeV machine (11.3 MW). Where necessary, comments concerning the 800 GeV upgrade (17.5 MW beam power) are included.

E_0 , particle energy	250 GeV	400 GeV
N_t , particles per bunch train	$5.64 \cdot 10^{13}$	$6.84 \cdot 10^{13}$
ν_{rep} , repetition rate	5 Hz	4 Hz
I_{ave} , average beam current	45 μ A	43.8 μ A
W_t , energy per bunch train	2.3 MJ	4.4 MJ
P_{ave} , average beam power	11.3 MW	17.5 MW

Table 7.7.1: Beam parameters relevant to the beam dump system for the 250 GeV main linac beam and its 400 GeV upgrade option.

7.7.1 Requirements and basic concept

The important beam parameters relevant to the dump are given in table 7.7.1. The current high-luminosity parameter set represents a 50% increase in the average power requirement compared to the CDR parameters [83]. Solid dumps are ultimately limited by the thermal conductivity of the material, and already become technically difficult beyond several hundred kW of beam power: in the MW regime, therefore, the only reasonable and technically feasible solution is a water dump, which can handle the high power by a sufficient mass flow of water towards an external heat exchanger [87].

Figure 7.7.1 shows the conceptual layout of the main parts of the dump system. The same dump is used for the main spent beam, and for the fast emergency extraction line (FEXL), described in section 7.2.6 (the main extraction line is described in section 7.6); as a result the dump requires an entrance window at both ends of the water vessel. A single cooling system (per side) is intended to serve both the main spent beam dump and the beamstrahlung collimator (section 7.6.2); if a second IR is constructed, then the same cooling plant can also be used for the additional dumps, since the *total* power at any given time can never exceed the maximum single beam power.

7.7.2 Design of water vessel

Most of the beam power should go into the water and not into the mechanical container: hence the vessel must be built from a minimum amount of mechanically strong and corrosion resistant material, which in addition represents a small source of induced radioactivity. The dump consists of about 11 m³ of water, which is housed in a 10 m long (27.7 radiation length) cylindrical titanium vessel, with a radius of 60 cm (6.3 molière radii), and a wall thickness of 15 mm.

According to 250 GeV shower simulations using the MARS code, energy escaping from the absorber is at the 1–2% level, and is dominated by radial leakage. Since penetration of the shower varies only logarithmically with energy, we can assume that the leakage power out of the vessel and into the surrounding shielding scales approximately linearly with incident beam power: an increase of $\sim 50\%$ is therefore expected for the 800 GeV upgrade.

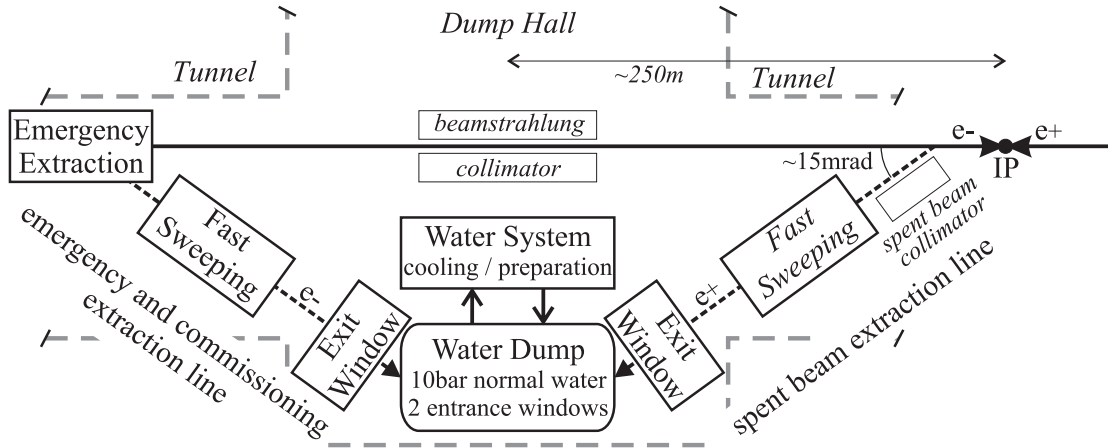


Figure 7.7.1: Schematic side view of the main linac beam dump system and its subcomponents.

Although relatively small, the leakage power is still more than 100 kW, and an inner shell of aluminum is required to significantly reduce the power density on the outer concrete shielding [86]. Aluminium was chosen because of its low residual radioactivity and high thermal conductivity. The removable shield will be thermally coupled to the water vessel. Gaps between the vessel and shielding, or within the shielding volume must be kept to a minimum to reduce air activation. For further details on radiation safety issues see section 8.3.

The absorption of all N_t particles of one bunch train leads to a certain energy distribution in the water, which directly translates into an instantaneous temperature rise with its maximum $(\Delta T_{inst})_{max}$ somewhere on the shower axis. If E_0 , N_t and the absorber material are fixed, $(\Delta T_{inst})_{max}$ only depends on the area of the incoming beam. The risk of boiling is avoided by:

- pressurising the water to 10^6 Pa (10 bar), which pushes the boiling point to about 160°C; and
- limiting the instantaneous temperature rise to $< 40^\circ$ C (assuming that the water has a temperature of $\sim 50^\circ$ C before the arrival of the beam).

The latter constraint sets a minimum RMS beam radius at the dump of 19 mm and 30 mm for $E_{beam} = 250$ GeV and 400 GeV respectively. For an *undisrupted* beam (i.e. no collision), the RMS beam size at the dump is only 1×0.4 mm² which is far too small: therefore the effective spot size has to be increased by using a fast sweeping system [88], that distributes all the bunches of the bunch train around a circle of radius 5 cm at 250 GeV (8 cm at 400 GeV) on the face of the dump. The fast sweeping system consists of a set of orthogonal deflectors excited with a sinusoidal current of the same frequency but with a 90° phase shift. The frequency needs to be at least 1 kHz in order to evenly

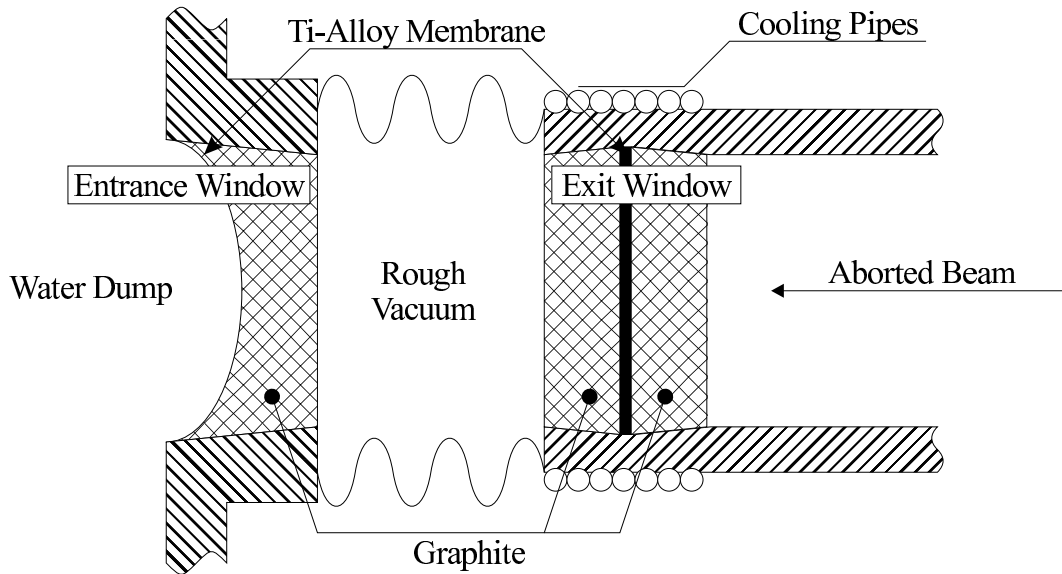


Figure 7.7.2: Concept of the (vacuum) exit and (water) entrance window, which is based on a titanium-graphite sandwich design.

distribute all the bunches from a single bunch train (950 μsec). Pulsed iron yoke dipoles sitting outside of the vacuum chamber will be used. Several independent modules in each plane are foreseen to allow safe operation should one fail. As an additional safety measure, the sweeper system will be triggered early enough to prevent the extraction of the bunch train from the damping ring should a failure in the system be detected.

7.7.3 Entrance and exit windows

Figure 7.7.2 shows the concept of the dump window. The beam passes through an exit window at the end of the vacuum system before it enters the water absorber through a second (separate) window: using two windows provides a level of redundancy in the event of a leak. The volume between the two windows requires a rough vacuum to avoid air activation. Windows for pulsed beams suffer from cyclic mechanical stress due to instantaneous heating. A 5 Hz operation and a 10 year lifetime gives in total about 10^9 cycles. Normally materials with high specific heat like beryllium are preferred; but given the required high number of cycles titanium alloys are good candidates. Available data for such alloys shows that the maximum allowed particle density $(dN/dA)_{max}$ at the window as a function of the number of cycles (before failure) tends to a constant value of $\sim 4 \times 10^{12} / \text{mm}^2$ after $\sim 10^4$ cycles [89]. Unfortunately data only exists up to 10^7 – 10^8 cycles. However, even for the undisrupted beam, the particle density on the window is a factor of ten less than this limit due to the constraint from the instantaneous temperature rise of the water.

The titanium membranes in both windows are reinforced by graphite disks as shown

in figure 7.7.2. In the case of the (vacuum) exit window, the graphite (which is located on either side of the membrane) will help to conduct away the average power¹ of 30 W/mm^2 towards the heat sink at the circumference of the window. For the (water) entrance window, average heating is not a problem since the membrane is cooled directly from the dump water.

The performance of the window is only dependent on the peak particle density and average beam current, and *not* on the beam energy: therefore, the window can also be used for the 800 GeV upgrade, since the average beam current remains roughly the same, and due to the increased sweep radius, the peak particle density is also approximately constant. Since the performance is not energy dependent, experience can be obtained from tests at the TESLA Test Facility Phase 2 (TTF2), where such a graphite-titanium sandwich-like window will be installed as an exit window.

7.7.4 Water system

Removal of the heat dissipated by the beam in the water vessel will be done by a special water in- and outlet system. The flow of water through the vessel is dictated by two constraints:

- to renew the volume of water that the shower sees for each beam pulse, a flow of $\sim 0.5 \text{ m/s}$ perpendicular to the shower axis (at the critical longitudinal position) must be guaranteed; and
- a continuous (bulk) flow of 100 kg/s , or $360 \text{ m}^3/\text{h}$ of water towards an external heat exchanger is required to handle the average power.

The temperature drop between in- and outlet is $\sim 30^\circ \text{ C}$. The heat exchanger is part of an ambitious water preparation plant, schematically shown in figure 7.7.3; the system must also handle the radiological and chemical aspects of the dump water.

It is expected that the dump water will remain in the closed system for the entire lifetime of the collider. For pure water, The following radioactive nuclei will be produced (half-life in brackets): ^{15}O (2 minutes); ^{13}N (10 minutes); ^{11}C (20 minutes); ^7Be (54 days); and ^3H (12 years). The activity of the ^7Be and ^3H saturate at 66 TBq and 7.3 TBq respectively. After decay of the short-lived isotopes, the outside dose rate is mainly determined by the 478 keV γ particles from the ^7Be decay, since the 20 keV electrons from tritium decay will not penetrate the walls of the water system. If distributed evenly in a total water volume of 10 m^3 , the estimated dose rate at the surface of a 300 mm diameter tube is about 500 mSv/h ; this value will be reduced by two to three orders of magnitude if a few percent of the total water flow is passed through a resin filter which removes the ^7Be . In addition, the filter removes other particles and therefore maintains the purity of the water, which is essential for avoiding corrosion. Radiolytical damage of the filter material is reduced by a delay line in front of the filter to allow the short-lived products to decay.

¹Assuming an average current of $45 \mu\text{A}$

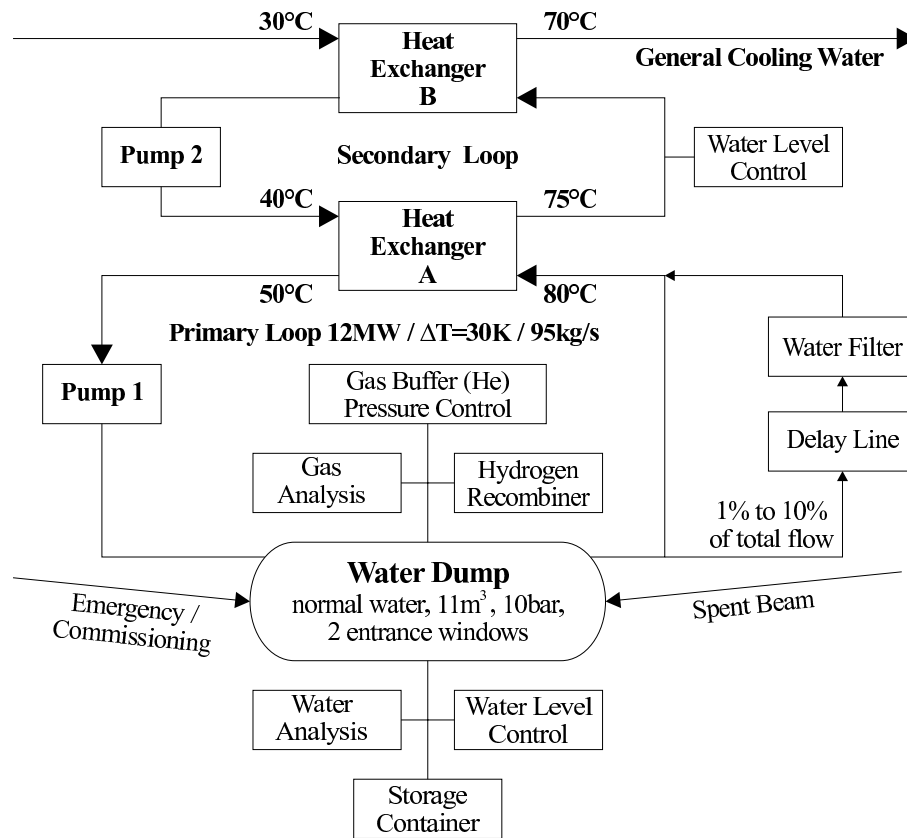


Figure 7.7.3: Schematic overview of the water system required for the main beam dump.

There will be a small gas volume (most probably He) at the top of the dump vessel; it will protect the vessel from pressure waves induced by instantaneous heating in the event of a failure of the fast sweeping system. The gas buffer will also maintain the static pressure and compensate for slow expansion due to different average temperatures of the dump water. All gaseous constituents not dissolved in the water will accumulate in the buffer: special attention must be paid to hydrogen, which is produced via radiolysis with a rate of 3.61/s [85]. A catalytic hydrogen recombiner and a gas analyzing station will be connected to the buffer volume.

The system needs to be leak-tight at the level typically found in vacuum systems; this requires gas-tight components (pumps, heat exchangers, etc.), welded or metal sealed connections, and a proper choice of materials to avoid harmful water-chemical reactions. A water analysis station will monitor relevant parameters such as acidity, ion concentrations and conductivity. However the possibility of a leak requiring a repair or exchange of a component has to be foreseen. Once a leak has been detected by monitoring water pressure and level, the system will first be flushed into the storage container to remove the dominant source of radiation, allowing work to proceed on the necessary mechanical parts after a relatively short cool-down period.

All walls of the hall for the system have to be sealed with a special paint to collect leaking water. The primary cooling circuit is separated from the the general cooling

water by an intermediate secondary loop, which has a higher pressure than the primary one. The loop protects the general cooling water from being contaminated, in the event of leaks in either of the heat exchangers. The whole water system will be housed in the dump hall.

The design and fabrication of such a complex water dump represents a significant technical challenge. However, similar systems already exist: e.g. the 25 GeV, 2.2 MW water dump at SLAC [84]; spallation neutron sources like the SINC at Paul Scherrer Institute (PSI); or research reactors. By using the experience gained at these and other facilities, a safe and technically feasible design can be achieved.

Bibliography

- [1] R. Brinkmann, G. Materlik, J. Roßbach and A. Wagner (eds.), *Conceptual Design of a 500 GeV e+e- Linear Collider with Integrated X-ray Laser Facility*, DESY-97-048 and ECFA-97-182, chapter 3: <http://www.desy.de/lc-cdr/tesla/tesla.html>, 1997.
- [2] J. Payet, O. Napoly, *A Proposal for the TESLA High Energy Switchyard*, DESY TESLA-2000-24, 2000.
- [3] R. Brinkmann, N. Walker, G. Blair, *The TESLA Post-linac Collimation System*, DESY TESLA-01-12, 2001.
- [4] M. D. Woodley, P. E. Emma, *Measurement and Correction of Cross Plane Coupling in Transport Lines*, Proc. 20th Int. Linac Conference, Monterey, CA, Aug. 2000, LINAC2000-MOC19, SLAC-PUB 8581, 2000.
- [5] K. Wittenberg, *Conventional Wire Scanners for TESLA*, DESY TESLA-00-18, 2000.
- [6] W. Inman et al., *A Laser-Based Beam Profile Monitor for the SLC/SLD Interaction Region*, Nucl. Instrum. Meth. **A379** (1996) 363.
- [7] K. L. Brown, *Basic Optics of the SLC Final Focus System*, presented at Workshop on Physics of Linear Colliders, Capri, Italy, June 1988, and Int. Workshop on the Next Generation of Linear Colliders, Stanford, CA, Nov. 1988, SLAC-PUB-4811, 1988.
- [8] D. Burke for the FFTB Collaboration, *Results from the Final Focus Test Beam*, Proc. 4th EPAC, London 1994, Vol. I, p. 23.
- [9] V. Sytchev et al., *Concept of an Emergency Extraction Kickersystem for TESLA*, DESY TESLA-01-06, 2001.
- [10] O. Napoly, J. Payet, N. Walker, *Emergency Extraction High-Energy Beamline for TESLA*, DESY TESLA-01-13, 2001.

-
- [11] E. Bondarchuk et al., *A Technical Proposal for the Development and Manufacturing of the Electromagnets for the TESLA BDS*, DESY TESLA-00-23, 2000.
- [12] E. Bondarchuk et al., *A Technical Proposal for the Development and Manufacturing of the Electromagnets for the TESLA Fast Emergency Extraction Line*, DESY TESLA-01-20, 2001.
- [13] E. Bondarchuk et al., *A Technical Proposal for the Development and Manufacturing of the Electromagnets for the TESLA Main Extraction Line*, DESY TESLA-01-21, 2001.
- [14] A. Brenger et al., *The Vacuum System for the TESLA Beam Delivery System*, DESY TESLA-01-14, 2001.
- [15] A. Sery, O. Napoly, *Influence of Ground Motion on the Time Evolution of Beams in Linear Colliders*, Phys. Rev. **E 53** no. 5 (1996) 5323.
- [16] N. Walker, A. Wolski, *Luminosity Stability Issues for the TESLA Beam Delivery System*, DESY TESLA-00-22, 2000.
- [17] F. Rouse, T. Gromme, W. Kozanecki, N. Phinney, *Maintaining Micron Size Beams in Collision at the Interaction Point of the Stanford Linear Collider.*, Proc. IEEE Particle Accelerator Conf., San Francisco, CA, May 1991, IEEE 1991:3222-3224 (QCD183:P3:1991), SLAC-PUB-5512, 1991.
- [18] D. Schulte, *Beam-Beam Simulations with Guinea-Pig*, CERN-PS-99-14, CERN-CLIC-NOTE-387, 1999.
- [19] C. Magne, M. Wendt, *Beam Position Monitors for the TESLA Accelerator Complex*, DESY TESLA-00-41, 2000.
- [20] F. Obier, *TTF Feedback Kicker*, DESY-M-002, 2000.
- [21] J. Rümmler, *Kicker Systems for the TESLA Transverse Feedback*, DESY-M-003, 2000.
- [22] I. Reyzl, *Stabilisation of Beam Interaction at the TESLA Linear Collider*, Proc. 7th EPAC, Vienna 2000, p. 315.
- [23] V. Shiltsev et al., *Measurements of Ground Vibrations and Orbit Motion at Hera*, DESY-HERA-95-06, 1995.
- [24] C. Montag, *Active Stabilization of Mechanical Quadrupole Vibrations for Linear Colliders*, Nucl. Instrum. Meth. **A378** (1996) 369.
- [25] B. A. Baklakov et al., INP 91-15; Tech. Ph. **38** (1993).
- [26] P. Tenenbaum et al., *Beam Based Alignment of the Final Focus Test Beam*, Proc. 4th International Workshop on Accelerator Alignment (IWAA95), Tsukuba 1995, p. 393; SLAC-PUB-7058, 1995.

-
- [27] N. Walker, *Linear Tuning and Estimates for the Initial Beam Based Alignment Requirements for the TESLA Beam Delivery System (BDS)*, DESY TESLA-00-29, 2000.
- [28] H.-J. Eckoldt, *Magnet Power supplies for Tesla*, DESY TESLA-00-37, 2000.
- [29] O. Napoly et al., *Beam-beam effects at the TESLA Linear collider*, DESY TESLA-01-15, 2001.
- [30] O. Napoly, D. Schulte, *Luminosity monitor options for TESLA*, Proc. 19th Int. Linac Conference, Chicago, Illinois, Aug. 1998, CERN-OPEN-2000-135 (1998).
- [31] O. Napoly, *Luminosity Stability, Possible Feedback, and Background at Future Linear Colliders*, Proc. 7th EPAC, Vienna 2000, p. 53.
- [32] R. Brinkmann, O. Napoly, D. Schulte, *Beam-Beam Instability driven by Wakefield Effects in Large Disruption Linear Colliders, to be published as DESY TESLA-01-16, 2001.*
- [33] A. Devred et al., *Conceptual Design for the Final Focus Quadrupole Magnets for TESLA*, DESY TESLA-01-17, 2001.
- [34] T. Shintake et al., *Experiments of Nanometer Spot Size Monitor at FFTB using Laser Interferometry*, Proc. Particle Accelerator Conf., Dallas 1995, Vol. 4, p. 2444.
- [35] O. Napoly, *Collimation Depth Requirements for the TESLA IR*, DESY TESLA-01-18, 2001.
- [36] R. Brinkmann et al., *The TESLA Beam Collimation System*, DESY TESLA-95-25, 1995.
- [37] M.C. Ross et al., *Single Pulse Damage in Copper*, Proc. 20th Int. Linac Conf., Monterey, CA, August 2000 (LINAC2000-MOA06); SLAC-PUB-8605, 2000.
- [38] P. Tenenbaum et al., *Direct Measurement of Geometric Wakefields from Tapered Rectangular Collimators*, Proc. 20th Int. Linac Conf., Monterey, CA, August 2000 (LINAC2000-MOA09); SLAC-PUB-8563, 2000.
- [39] E. Merker et al., *The TESLA High-Power Extraction Line*, DESY TESLA-2001-19, 2001.
- [40] B. Balhan, B. Goddard, M. Sassowsky, *Engineering Considerations for the Proposed Beam Extraction System at TESLA*, CERN Preprint, SL-Note-2000-002 MS, 2000.
- [41] R. B. Neal et al., *The Stanford Two-Mile Accelerator*, chapter 20-2 W. A. Benjamin Inc., New York, 1968.

-
- [42] D. R. Walz, E. J. Seppi, *Radiolysis and Hydrogen Evolution in the A-Beam Dump Radioactive Water System*, SLAC-TN-67-29, 1967.
- [43] D. Dworak, J. Łoskiewicz, *Direct Energy Deposition in the Lateral Concrete Shielding of the TESLA Water Dump and the Rise of Shielding Temperature*, Report No 1854 / PH, The Henryk Niewodniczański Institute of Nuclear Physics, Kraków, Poland, 2000.
- [44] [M. Maslov et al.](#), *Concept of the High Power e^\pm Beam Dumps for TESLA*, DESY TESLA-01-04, 2001.
- [45] [V. Sytchev et al.](#), *Concept of the Fast Beam Sweeping System for the e^\pm Beam Dumps of TESLA*, TESLA 2001-05, 2001.
- [46] [M. Maslov et al.](#), *Concept of Beam Entrance and Exit Windows for the TESLA Water based Beam Dumps and its related Beamlines*, DESY TESLA-01-07, 2001.

